

IMPROVING REGIONAL HYDROLOGY FORECASTING FOR THE NORTH CENTRAL
TEXAS REGION UTILIZING CONDITIONAL ENSEMBLE STREAMFLOW
AND HYDROMETEOROLOGICAL CONDITION PREDICTIONS
WITH ARTIFICIAL NEURAL NETWORK MODELING

by

TYLER FINCANNON

Presented to the Faculty of the Graduate School of
The University of Texas at Arlington in Partial Fulfillment
of the Requirements
for the Degree of
MASTER OF SCIENCE IN ENVIRONMENTAL AND EARTH SCIENCE

THE UNIVERSITY OF TEXAS AT ARLINGTON

MAY 2017

Copyright © by Tyler Fincannon 2017

All Rights Reserved



Acknowledgements

This research could not have been accomplished without the contributions and support of a multitude of individuals and organizations. I would first like to acknowledge the National Oceanic Atmospheric Administration (Award Nr.:NA15OAR4310109) and The University of Texas at Arlington for providing both the funding and the resources to make this research possible. I also would like to extend my gratitude to my graduate advisor Dr. Arne Winguth for providing the opportunity to work alongside him. Under his guidance, I was given both the support and encouragement that was fundamental in the construction of this thesis. I would also like to thank the members of my graduate committee Dr. Elizabeth Griffith and Dr. Merlynd Nestell for their time and contributions on this project. I would also like to acknowledge Dr. D.J. Seo and Dr. Sunghee Kim, from the Department of Civil Engineering, for their collaboration and assistance on this research project.

On a personal note, I must express my gratitude to my parents Ann and David Fincannon, and my brother Patrick for their unending support in pursuing higher education. Furthering my education would never have been possible without the solid foundation my family instilled in me. Additionally, I would like to thank my co-worker Dr. Taylor Hughlett for providing me the benefit of her experience and helping me throughout graduate school.

April 14, 2017

Abstract

IMPROVING REGIONAL HYDROLOGY FORECASTING FOR THE NORTH CENTRAL TEXAS REGION UTILIZING CONDITIONAL ENSEMBLE STREAMFLOW AND HYDROMETEOROLOGICAL CONDITION PREDICTIONS WITH ARTIFICIAL NEURAL NETWORK MODELING

Tyler Fincannon, MS

The University of Texas at Arlington, 2017

Supervising Professor: Arne Winguth

The predictive skill of hydrologic variables such as streamflow and soil moisture, in North Central Texas, has improved substantially in the recent decades. However, substantial model-data biases are still present during extreme climate events, such as droughts and flash floods. In this study, we have optimized the Hydraulic Ensemble Forecasting System (HEFS) through development of a conditional ensemble streamflow system, as well as forecast reservoir hydrometeorological conditions (e.g. drought indices) with an artificial neural network (ANN) model. Improving prediction of these reservoir conditions enables more effective reservoir management in terms of water resource and energy efficiency during regional weather and climate anomalies. In order to improve HEFS, the strength of the regional climatology teleconnections to global climate indices (e.g. the Atlantic Multidecadal Oscillation, AMO, and the Bivariate El Niño Southern Oscillation, ENSO) was evaluated through Pearson product correlation, singular spectrum analysis, and the evaluation of the regional precipitation probability density and cumulative distributions functions in regards to changes in climate phases. These results showed the greatest change in regional precipitation base state occurred during changes in the AMO

phases, except in the case of an El Niño or La Niña event. This suggests that a conditional ensemble streamflow system could be constructed based on AMO phases to improve HEFS under regular conditions, and based on ENSO conditions (El Niño or La Niña events).

In the pursuit of forecasting hydrometeorological conditions, multiple ANN models of different network architectures were trained and tested utilizing data from 1915-2012; 70% of the available data, from 1915 to 1982, were used for model training and the remaining for validation. The network architecture that produced the smallest prediction error was applied further in this study. The input data comprised regional climate variability observations of minimum and maximum temperature, total precipitation, average wind speed, evapotranspiration, potential evapotranspiration, and the monthly drought index value. The global climate indices investigated included dominant interannual and decadal oscillations. These indices were used to evaluate their respective ability to improve predictive skill during climate anomaly extremes, e.g., El Niño and La Niña conditions. The choice of climate indices were varied as input into retrained ANN models of the same network architecture, so that the improvement due to each climate index could be ranked and less-influential climate indices could be excluded. The selected ANN model architecture and input data mentioned above were then applied to produce 6 month-ahead predictions of monthly drought indices in order to evaluate the overall predictive skill of the generated ANN models. The ANN model was able to skillfully forecast drought conditions with 2-3 months lead time, with the evaporation variables generating the greatest increase in forecasting skill. The use of global climate indices did not exhibit any increase in the ANN models' forecasting skill of North Central Texas regional hydrometeorological conditions most likely because the local observations consist of a regional signal that is superimposed by the global variations.

Table of Contents

Acknowledgements	iii
Abstract	iv
Figures	viii
Tables.....	xiii
Chapter 1 Introduction.....	1
1.1 Climate Anomalies and Extreme Weather Events in North Central Texas	1
1.2 Tarrant Regional Water District (TRWD)	4
Chapter 2 Objective	7
2.2 Conditional Ensemble Streamflow Prediction	7
2.3 Hydrometeorological Forecasting	8
Chapter 3 Methodology	9
3.1 Global Climate Indices.....	9
3.1.1 Introduction	9
3.1.2 Climate Index Datasets	15
3.2 Conditional Ensemble Streamflow Prediction	16
3.2.1 North Central Texas Regional Climate Anomalies	16
3.2.2 Computation of Climate Anomalies and Normalization	19
3.2.3 Moving Average Filter	20
3.2.4 Blackman-Turkey Spectrum Analysis.....	21
3.2.5 Correlations and Cross-Correlations	21
3.2.6 Empirical Cumulative Distribution and Probability Density Function	22

3.3 Hydrometeorological Forecasting	22
3.3.1 Potential Evapotranspiration	23
3.3.2 Standardized Precipitation Evapotranspiration Index	24
3.4 Artificial Neural Network (ANN) Model	27
3.4.1 Introduction	27
3.4.2 Model Description	28
Chapter 4 Conditional Ensemble Streamflow Prediction	32
4.1 Results	32
4.1.1 Regional Climate Anomalies and Global Climate Indices Correlations	32
4.1.2 Spectral Analysis	33
4.1.3 Empirical Cumulative Distribution Function and Probability Density Function Analysis	38
4.2 Discussion	39
Chapter 5 Hydrometeorological Forecasting	52
5.1 Artificial Neural Network (ANN) Model Results	52
5.2 Discussion	57
Chapter 6 Conclusion	66
References	68
Biographical Information	76

Figures

Figure 1: Annual average precipitation of Trinity River Basin reservoir catchments calculated from average rainfall from 1980-2010 in ArcGIS. Precipitation data provided by the PRISM Climate group (CITE). Reservoir catchment stations ID's labeled in figure.	2
Figure 2: Water supply network of the Tarrant Regional Water District as of January, 2017. Adapted from [Sunghee <i>et al.</i> , 2016].	3
Figure 3: Schematic of Hydraulic Ensemble Forecasting System incorporation in the Community Hydrologic Prediction System environment. Dark grey boxes represent ensemble-specific components while light gray boxes utilize single-valued forecasting. Adapted from [Demargne <i>et al.</i> , 2014].	4
Figure 4: Texas climate divisions utilized by the National Climate Data Center and National Weather Service when outputting regional drought indices [Gilbeaux, 2013].	6
Figure 5: Sea surface temperatures (SST) derived from January mean values with positive AMO phases on the left and negative AMO phases on the right. Adapted from [Yamamoto and Palter, 2016].	10
Figure 6: Atlantic Multidecadal Oscillation over North America. Gray shading represents negative precipitation anomaly, diagonal slashes positive precipitation anomaly. Adapted from [Hu <i>et al.</i> , 2011].	11
Figure 7: Sea surface temperature deviation in color, sea level pressures represented with contours, and surface wind stress with arrows. Adapted from [Mantua <i>et al.</i> , 1997].	13
Figure 8: Regions of averaged sea surface temperature to evaluate ENSO conditions. Provided from [NOAA, 2017].	14
Figure 9: North American climate patterns during La Niña and El Niño conditions. Provided from [NOAA, 2016].	15

Figure 10: Map of the locations of the KDWF stations operated by the National Weather Service from 1898 to present.	17
Figure 11: Time series of the standardized precipitation evapotranspiration index (SPEI) for reservoir catchment SGET2 and for time steps 3, 6, and 12 months.	26
Figure 12: The structure of a mammalian neuron. Adapted from [<i>Furber and Temple</i> , 2007].	28
Figure 13: Artificial neural model forecasting skill in relation to the variation of the number of hidden neurons. Optimum architecture identified as 4 hidden neurons.	30
Figure 14: Artificial neural network model architecture with a gaussian symmetric activation function. Model inputs were varied to determine input importance in forecasting for climate indices, evaporation variables, temperature, and precipitation.	31
Figure 15: Pearson correlation between temperature anomaly (T) and precipitation anomaly (P) of stations in North Central Texas (Dallas Fort Worth Airport, DFW, and WF Trinity R NR Jacksboro station, JAKT2) and major climate indices (AMO, PDO, SOI, NAO) during El Niño climate conditions, along with a representative histogram of each correlated variable.	34
Figure 16: Pearson correlation between temperature anomaly (T) and precipitation anomaly (P) of stations in North Central Texas (Dallas Fort Worth Airport, DFW, and WF Trinity R NR Jacksboro station, JAKT2) and major climate indices (AMO, PDO, SOI, NAO) during La Niña climate conditions, along with a representative histogram of each correlated variable.	35
Figure 17: Singular spectrum analysis of global climate indices and regional climate anomalies: A) AMO power spectrum with a 650 discrete Fourier transform (DFT) bin window, B) PDO power spectrum with a 650 DFT bin window, C) DFW precipitation anomaly power spectrum with a 650 DFT bin window and annual moving average filter,	

D) ENSO power spectrum with a 126 DFT bin window, E) DFW temperature anomaly power spectrum with a 650 DFT bin window and annual moving average filter..... 37

Figure 18: Probability density function (left) and cumulative distribution function (right) of total annual precipitation (in) from 1915-2012 for Trinity River Basin reservoirs during positive (red) and negative (blue) AMO phase years without La Niña and El Niño events. Note that 1 in = 25 mm..... 43

Figure 19: Probability density function (left) and cumulative distribution function (right) of total annual precipitation (in) from 1915-2012 for Trinity River Basin reservoirs during positive (red) and negative (blue) La Niña and El Niño event years. Note that 1 in = 25 mm. 44

Figure 20: Probability density function (left) and cumulative distribution function (right) of total annual precipitation (in) from 1915-2012 for Trinity River Basin reservoirs during positive (blue) and negative (red) PDO phase years. Note that 1 in = 25 mm. 45

Figure 21: Probability density function (left) and cumulative distribution function (right) of total winter (Dec-Feb) precipitation (in) from 1915-2012 for Trinity River Basin reservoirs during positive (red) and negative (blue) AMO phase years without La Niña and El Niño events. Note that 1 in = 25 mm. 46

Figure 22: Probability density function (left) and cumulative distribution function (right) of total winter (Dec-Feb) precipitation (in) from 1915-2012 for Trinity River Basin reservoirs during positive (red) and negative (blue) La Niña and El Niño event years. Note that 1 in = 25 mm. 47

Figure 23: Probability density function (left) and cumulative distribution function (right) of total winter (Dec-Feb) precipitation (in) from 1915-2012 for Trinity River Basin reservoirs during positive (blue) and negative (red) PDO phase years. Note that 1 in = 25 mm. 48

Figure 24: Probability density function (left) and cumulative distribution function (right) of total spring (Mar-May) precipitation (in) from 1915-2012 for Trinity River Basin reservoirs during positive (red) and negative (blue) AMO phase years without La Niña and El Niño events. Note that 1 in = 25 mm.	49
Figure 25: Probability density function (left) and cumulative distribution function (right) of total spring (Mar-May) precipitation (in) from 1915-2012 for Trinity River Basin reservoirs during positive (red) and negative (blue) La Niña and El Niño event years. Note that 1 in = 25 mm.	50
Figure 26 Probability density function (left) and cumulative distribution function (right) of total spring (Mar-May) precipitation (in) from 1915-2012 for Trinity River Basin reservoirs during positive (blue) and negative (red) PDO phase years. Note that 1 in = 25 mm.	51
Figure 27: Tarrant Regional Water District reservoir catchment stations. Stations used in ANN modeling marked in red.	54
Figure 28: Brier's forecast skill score against climatology in regards to input variables such as temperature (red), precipitation (blue), and evaporation variables (brown). Also shown is the skill score using global climate indices only (green; AMO, PDO, ENSO) and total forecast using positive skill variables (black).	55
Figure 29: SPEI 6 month drought index values for reservoir catchment SGET2 from 1983-2012 with black representing actual values and red the ANN model 1 month in advance predicted values.	60
Figure 30: SPEI 6 month drought index values for reservoir catchment SGET2 from 1983-2012 with black representing actual values and red the ANN model 2 month in advance predicted values.	61

Figure 31: SPEI 6 month drought index values for reservoir catchment SGET2 from 1983-2012 with black representing actual values and red the ANN model 3 month in advance predicted values.	62
Figure 32: SPEI 6 month drought index values for reservoir catchment SGET2 from 1983-2012 with black representing actual values and red the ANN model 4 month in advance predicted values.	63
Figure 33: SPEI 6 month drought index values for reservoir catchment SGET2 from 1983-2012 with black representing actual values and red the ANN model 5 month in advance predicted values.	64
Figure 34: SPEI 6 month drought index values for reservoir catchment SGET2 from 1983-2012 with black representing actual values and red the ANN model 6 month in advance predicted values.	65

Tables

Table 1: Data collection stations provided and operated by the United States Geologic Survey and the National Weather Services for the Trinity River Basin. Station coordinates, area coverage, elevation, date of data collection, and type of data collection are provided in table.....	18
Table 2: Pearson correlation coefficient (R) and significance test (p-value) between temperature anomaly (T) and precipitation anomaly (P) of stations in North Central Texas (Dallas Fort Worth Airport, DFW, and WF Trinity R NR Jacksboro station, JAKT2) and major climate indices (AMO, PDO, SOI, NAO) during El Niño and La Niña climate conditions. Note that $p < 0.05$ (red) denotes statistical significance.....	36
Table 3: Model forecasting mean absolute error (MAE) and Pearson R^2 coefficient of determination for all SPEI conditions and moderate to extreme drought conditions (SPEI < -1.0).....	56

Chapter 1

Introduction

1.1 Climate Anomalies and Extreme Weather Events in North Central Texas

The North Central Texas region is affected by climate anomalies and extreme weather events such as prolonged droughts and short term flooding events. These events negatively impact local water resources and result in weather-related fatalities by flash floods, wildfires, increased air pollutants, and significant economic damages, e.g. on transportation infrastructure and the energy sector [*Patricola et al.*, 2013; *Stahle and Cleaveland*, 1998; *Winguth et al.*, 2015]. One example is the 1980 heat wave that generated 1.5 billion dollars in losses for Texas and 16 billion dollars in damages nationwide [*Karl and Quayle*, 1981]. Another example is the more recent 2011 drought that broke records from 1895 to present as the driest 12-month period in Texas from October 2010 to September 2011 with a record minimum of -7.93 on the Palmer Drought Severity Index, a measurement of relative dryness in regards to a departure from average precipitation [*Hoerling et al.*, 2013; *Palmer*, 1965]. The 2011 drought resulted in a state wide agricultural loss of \$7.62 billion dollars [*Fannin*, 2012]. These periodic droughts have been shown to have regular occurrences over a period of multiple years. For example, the probability of a moderate to severe June drought occurring in Texas over a period of 10 years is greater than 90 percent [*Stahle and Cleaveland*, 1998]. Droughts in the North Central Texas region reoccur with a low frequency that has attributes of a 30-year periodicity [*Ortegren et al.*, 2011]. Improving the forecasting ability in predicting when extreme climate events will recur could prevent the economic damages linked to these events. For example, advance preparations can be made for a drought-related reservoir storage, and for improving the efficiency in estimates of water and energy resources.

This project focused on the Tarrant Regional Water District (TRWD), which services the water needs of 2 million people in the North Central Texas region and operates the flood control system of Tarrant County [Newby and Oliver, 2016]. The TRWD relies on 4 major reservoirs in which surface water accounts for over 95% of the reservoir water input [Vaughan, 2012]. The reliance on surface water runoff to refill the reservoir system increases TRWD's susceptibility to climate anomalies, such as periods of moderate to extreme droughts. The TRWD also experiences a west-to-east precipitation gradient across its reservoir system, with the west side of the Trinity River Basin receiving an annual average of 254 mm (10 in) less of rainfall than the east side, as shown in Figure 1.

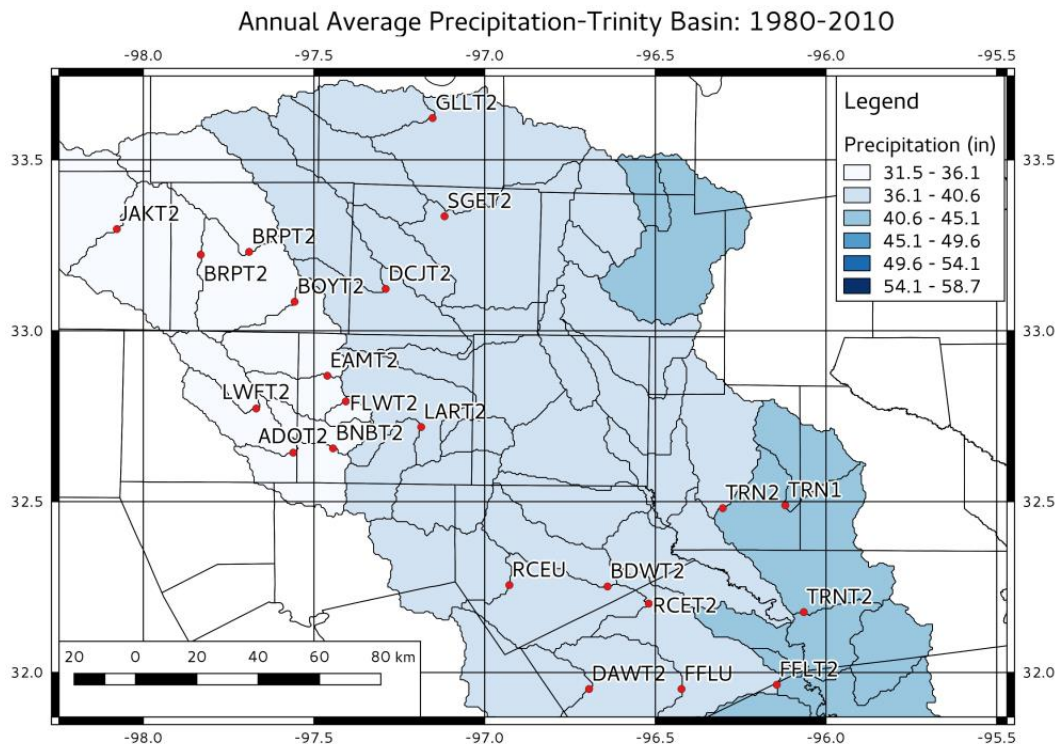


Figure 1: Annual average precipitation of Trinity River Basin reservoir catchments calculated from average rainfall from 1980-2010 in ArcGIS. Precipitation data provided by the PRISM Climate group (CITE). Reservoir catchment stations ID's labeled in figure.

As the DFW metroplex lies on the west side, of the Trinity River Basin, pipelines were constructed, as seen in Figure 2, to connect the west and east reservoir systems so that water accumulation on the east side of the Trinity River Basin could be pumped up an elevation grade to the western side to cover the water shortfalls in the metroplex during drought conditions.

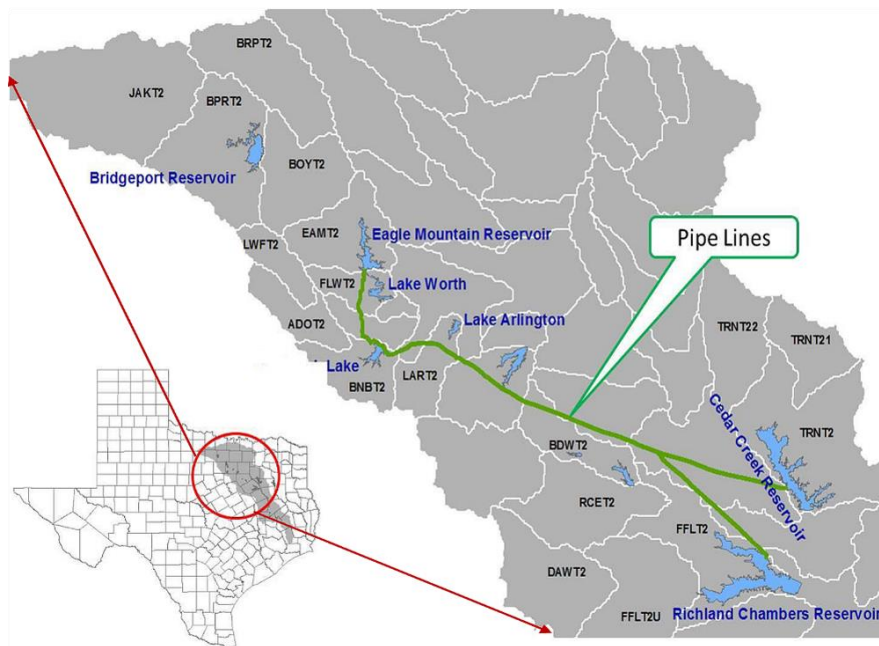


Figure 2: Water supply network of the Tarrant Regional Water District as of January, 2017. Adapted from [Sunghee *et al.*, 2016].

The TRWD would noticeably benefit from increased forecasting skill resulting in greater energy conservation because a more accurate prediction of reservoir levels may reduce the amount of water that must be pumped to the DFW metroplex to cover the municipalities' water demands. These savings could be significant as the TRWD estimates in 2017 23 million dollars will be spent on only the energy costs related to pumping for their pipeline system.

1.2 Tarrant Regional Water District (TRWD)

The TRWD has recently incorporated a river and reservoir modeling software tool named Riverware [Blaylock *et al.*, 2016] developed by the University of Colorado at Boulder, into their operational decision support network. The Riverware tool incorporates a Community Hydrologic Prediction System (CHPS) for forecasting future reservoir conditions. CHPS utilizes a Hydrologic Ensemble Forecast Service (HEFS, Figure 3), developed by the National Weather Service and their collaborators [Demargne *et al.*, 2014], which employs ensemble forecasting to generate probability statements about the likelihood of extreme future weather events.

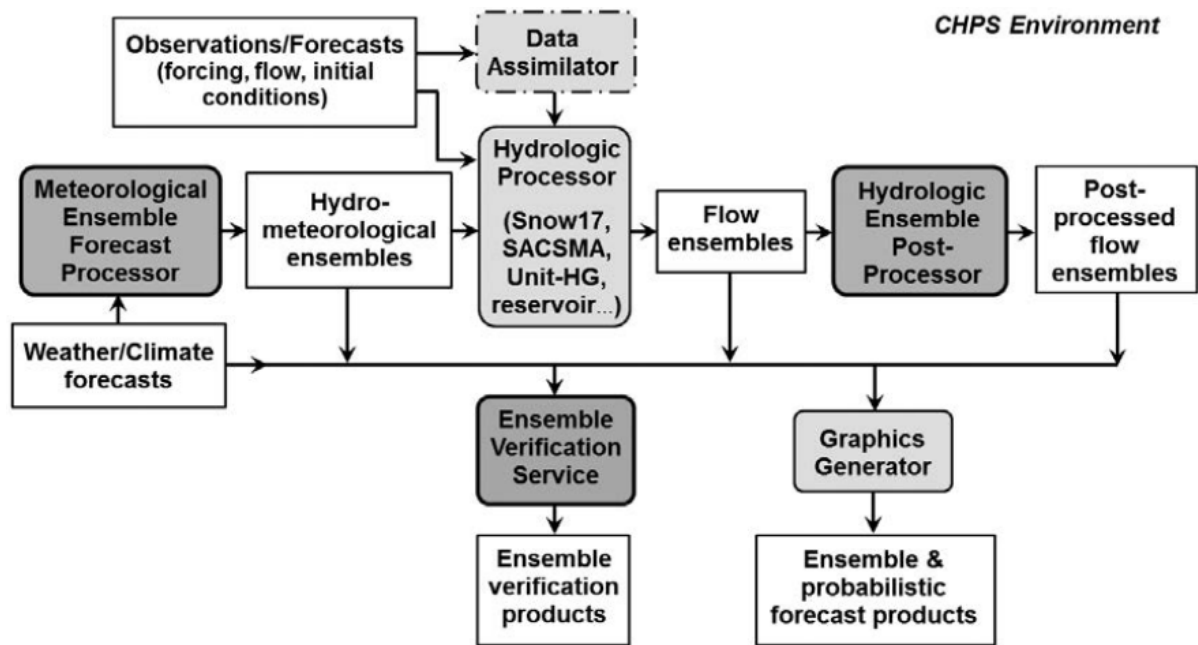


Figure 3: Schematic of Hydraulic Ensemble Forecasting System incorporation in the Community

Hydrologic Prediction System environment. Dark gray boxes represent ensemble-specific components while light gray boxes utilize single-valued forecasting. Adapted from [Demargne *et al.*, 2014].

The forecasting ability for hydrological systems generally has limited predictive skill when uncertainties are not compensated for. The uncertainty in forecasting arises from two main factors: uncertainty of the input data, such as atmospheric forcing and hydrological condition uncertainty (e.g. initial conditions and model parameters); and HEFS model structure uncertainty, such as whether the model's behavior accurately reflects the reality of hydrological conditions [Gupta *et al.*, 2006]. The HEFS system works to enhance the confidence levels in the forecasts by accounting for major sources of uncertainty [Demargne *et al.*, 2007] rather than previous models, which modelled total uncertainty to the output of the forecast [Montanari and Grossi, 2008]. These uncertainties are computed by the Hydrologic Ensemble Post-Processor system (EndPost) and subsequently corrected to form bias-corrected stream flow ensembles. The HEFS system also applies a meteorological ensemble forecast processor (MEFP), seen in Figure 3, to account for input uncertainties by producing bias-corrected forcing ensembles for the HEFS system. The MEFP improves in skill when utilizing reanalyzed data sets from frozen Numerical Weather Prediction Service (NWPS) models [Schaake *et al.*, 2007]. It should be noted, however, that a lack of observation records of extreme weather events would limit the ability to properly implement hindcast training for the model.

One of this project's focuses was to determine, if uncertainty of input data may be reduced and the meteorological ensemble forecasting optimized through the incorporation of a conditional Ensemble Streamflow Prediction (ESP) system. The system was constructed from the phase changes of teleconnected climate indices and their respective effect on regional precipitation [Hamlet and Lettenmaier, 2000]. The second objective of the project was to optimize the hydrometeorological conditions, such as whether persisting drought or wet conditions exist, for the reservoir catchment area by utilizing the Riverware decision support tool. Presently, TRWD utilizes a single drought index value supplied for

all of the North Central Texas region, outlined in Figure 4, for the hydrometeorological condition of all reservoir catchments within the TRWD system.

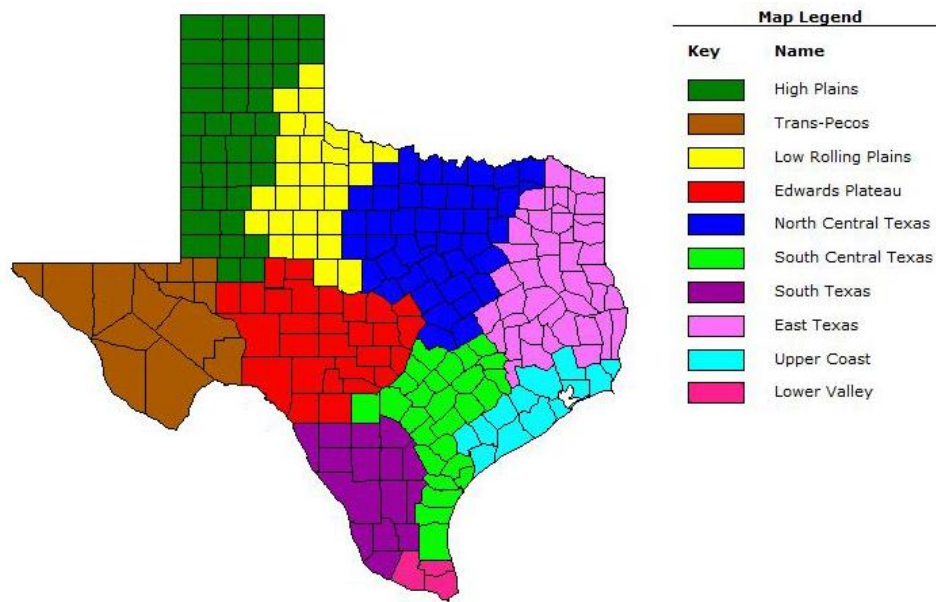


Figure 4: Texas climate divisions utilized by the National Climate Data Center and National Weather Service when outputting regional drought indices [*Gilbeaux, 2013*].

Chapter 2

Objective

2.1 Introduction

The purpose of the study was to research and develop potential methods that utilize regional climatology and global climate indices to improve current regional hydrologic forecasting utilized by the Tarrant Regional Water District. The methodology developed in this study can be implemented across multiple regional water districts to increase hydraulic forecasting. This study focused on two main improvements to TRWD's current hydraulic forecasting system:

1. The optimization of HEFS forecasting through determining which global climate indices are suitable to be developed into a conditional Ensemble Streamflow Prediction for HEFS, and
2. The development of an Artificial Neural Network (ANN) forecasting model utilizing global climate indices and regional climatology to determine future hydrometeorological conditions for individual reservoir catchments.

Detailed below are the steps that were taken to complete both improvements.

2.2 Conditional Ensemble Streamflow Prediction

As an initial step potential teleconnections were explored between the regional climatology of the DFW metropolis and the global climate indices of the Atlantic Multidecadal Oscillation (AMO), Pacific Decadal Oscillation (PDO), North Atlantic Oscillation (NAO), Southern Oscillation Index (SOI), and the El Niño Southern Oscillation

(ENSO). The impact of the teleconnections on the regional climate was then determined by correlations, between regional climate anomalies and global climate indices, as well as singular spectrum analysis. Climate indices with potential regional teleconnections were then further analyzed by the construction of regional probability density functions and cumulative distribution functions in regard to the global climate phase effect on annual and seasonal precipitation.

In a following step, the global climate indices which resulted in the largest precipitation discrimination on an annual and seasonal basis were determined by comparing differences in the precipitation probability density functions and cumulative distribution functions between respective climate phases. As such, climate indices were ranked based on their phase influence on regional precipitation.

2.3 Hydrometeorological Forecasting

The second main objective was the development of ANN forecast model to explore teleconnections between global and regional climate by predicting meteorological drought index values in relation to regional climatology and global climate indices. The ANN model utilized 4 main input categories as variables; climate indices (AMO, PDO, ENSO), evaporation variables (wind speed, potential evapotranspiration, and evaporation), minimum and maximum temperature, and precipitation. The ANN model's input and hidden neuron architecture was then varied to determine which meteorological variables and model design resulted in the lowest overall forecasting error for drought index values. Finally, the ANN model's forecasting skill against climatology was evaluated to determine the effectiveness in utilizing Artificial Neural Networks in the prediction of hydrometeorological conditions of our regional study area through drought index values.

Chapter 3

Methodology

3.1 Global Climate Indices

Climate indices are indicators of changes in climatological trends and short term climatological events. This study evaluated the incorporation of climate indices into regional hydrological predictions. The introduction section of this chapter introduces the primary climate indices used in this study as well as current research regarding their respective effects on North America climatology, while the climate index datasets section provides information necessary to obtain the climate index data used in this study.

3.1.1 Introduction

The Earth's climate system consists of the atmosphere, hydrosphere, cryosphere, biosphere, and lithosphere and variations between and within these components influence long-term fluctuations of temperature, precipitation, pressure, humidity, and wind. Indicators of climate variations are referred to as climate indices that can encompass e.g. changes in average sea surface temperature, pressure differences, wind, and precipitation rates. Through measurement of these changes over a time span exceeding 50 years, depending on the characteristic frequency of the fluctuations [Wyatt *et al.*, 2011], phases of increased variability and average period length can be determined. The climate indices this study considered are the Atlantic Multidecadal Oscillation (AMO) [Bjerknes, 1964], Pacific Decadal Oscillation (PDO) [Mantua *et al.*, 1997], North Atlantic Oscillation (NAO) [Hurrell and van Loon, 1997], Southern Oscillation Index (SOI) [Bjerknes, 1969], and the Bivariate El Niño Southern Oscillation (ENSO) [Schlesinger and Ramankutty, 1994].

The Atlantic Multidecadal Oscillation is the area weighted average sea surface temperature (SST) over the North Atlantic (0°N - 70°N) with a period oscillation of 65-70 years [Enfield, 2001]. This variability in sea surface temperature has been attributed to fluctuation in the thermohaline circulation and has been shown to be self-sustaining and independent of external forcing [Delworth and Mann, 2000]. It has been also linked to the variability of Greenland sea ice and of sea level pressure [Venegas and Mysak, 2000]. The AMO phases are shown on Figure 5 with the positive phase showing above average sea surface temperatures (SST) and the negative phase below average SST. The AMO index has been correlated to rainfall rates and modulate precipitation patterns in the US with positive (negative) phases of the AMO reducing (increasing) the amount of precipitation in the US [Enfield, 2001]. During the negative AMO phase, the North Atlantic subtropical high pressure system is strengthened, and an enhanced high pressure system develops over the

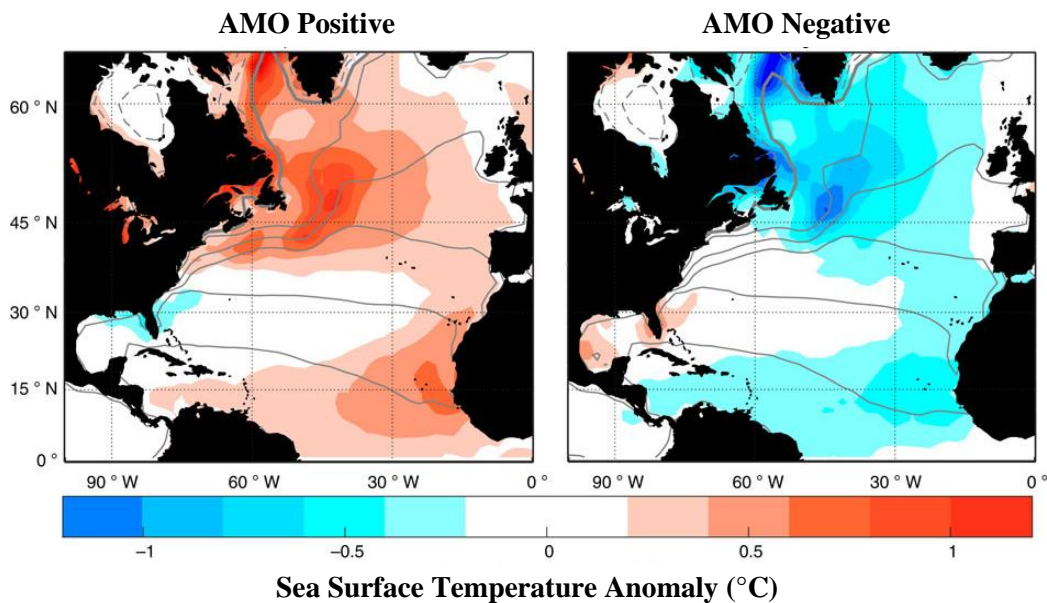


Figure 5: Sea surface temperatures (SST) derived from January mean values with positive AMO phases on the left and negative AMO phases on the right. Adapted from [Yamamoto and Palter, 2016].

western North American continent. These conditions develop into two anticyclonic cells, separated by the Sierra Madre Mountains as seen in Figure 6. The Gulf of Mexico anticyclonic cell brings moisture north and into the central United States region accounting for the increased precipitation during AMO cold phases. In contrast, during AMO positive

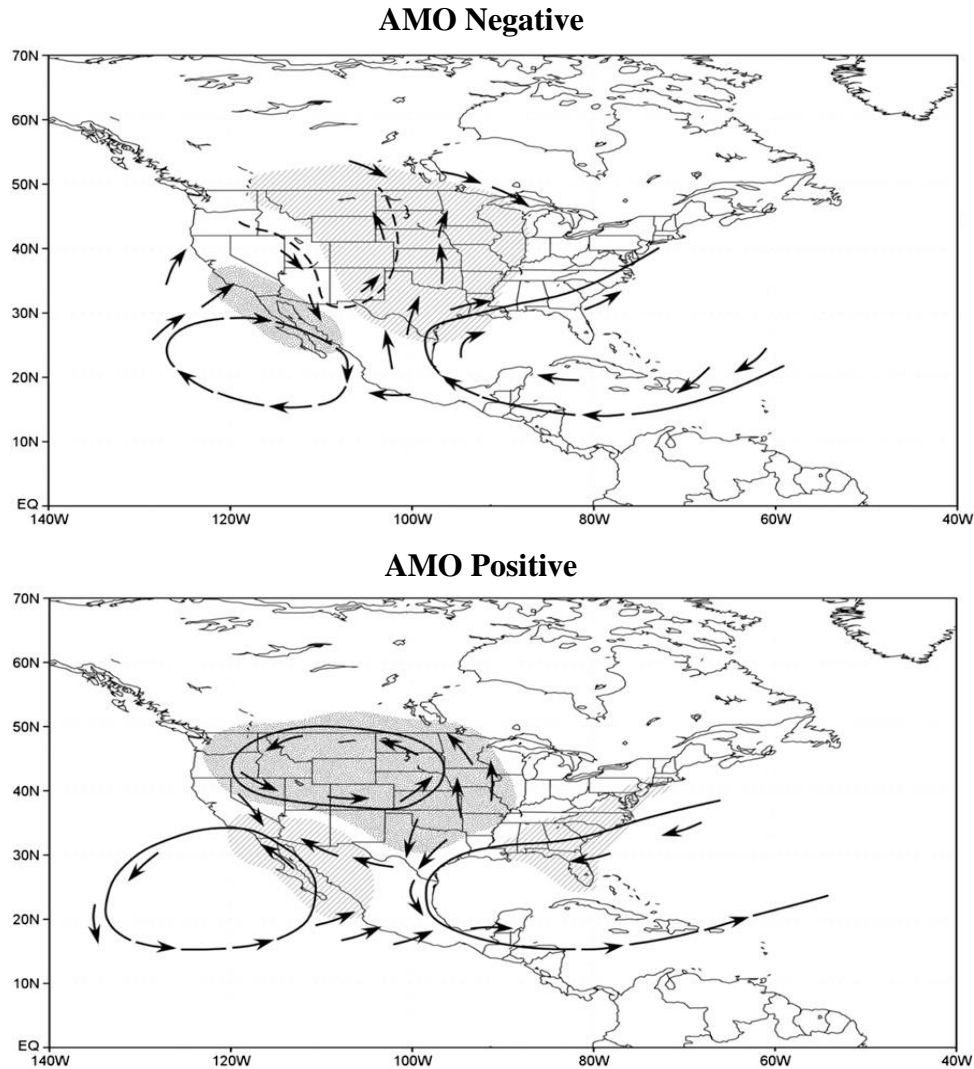


Figure 6: Atlantic Multidecadal Oscillation over North America. Gray shading represents negative precipitation anomaly, diagonal slashes positive precipitation anomaly. Adapted from [Hu *et al.*, 2011].

phase, the North Atlantic subtropical high pressure system contracts and is shifted eastward. This shift in the subtropical high pressure system generates cyclonic cells over the Gulf of Mexico and the West Pacific Ocean limiting the northward flow of moisture into the central United States resulting in lower precipitation during AMO warm phases.

The North Atlantic Oscillation is defined as pressure fluctuations between the Icelandic low pressure and the Azores high pressure [*van Loon and Rogers, 1978*]. Its phases are associated with changes in the westerly winds, which travel over the Atlantic to Europe. This oscillation accounts for more than 30% of the variance of sea level pressure in the Northern Atlantic [*Wallace and Gutzler, 1981*]. The positive phase of NAO represents stronger than average westerlies at the mid-latitudes and an associated lower-than-normal Icelandic low with the most pronounced signal in winter months [*Hurrell and van Loon, 1997*]. The pressure fluctuations are related to the changing strength of the Hadley cell in response to a positive SST anomaly. The NAO mainly influences winter precipitation patterns over Europe and the North America east coast [*Dai et al., 1997*].

The Pacific Decadal Oscillation shown in Figure 7 is comprised of sea surface temperature variations in the Pacific above 20°N, quantifying extra-tropical variability in the Pacific [*Mantua et al., 1997; Zhang et al., 1997*]. The PDO is constrained by two dominant oscillations that consists of a 15-25 year cycle, controlling the transition between positive and negative phases [*Minobe, 1997*], and a 50-70 year cycle. The variability in the PDO is teleconnected to the occurrences of shorter term El Niño and La Niña events from the atmospheric bridge created during the events. The teleconnection between the two indices result in the increase of La Niña events during negative PDO phases and El Niño events during positive phases [*Lapp et al., 2013*].

Pacific Decadal Oscillation (PDO)

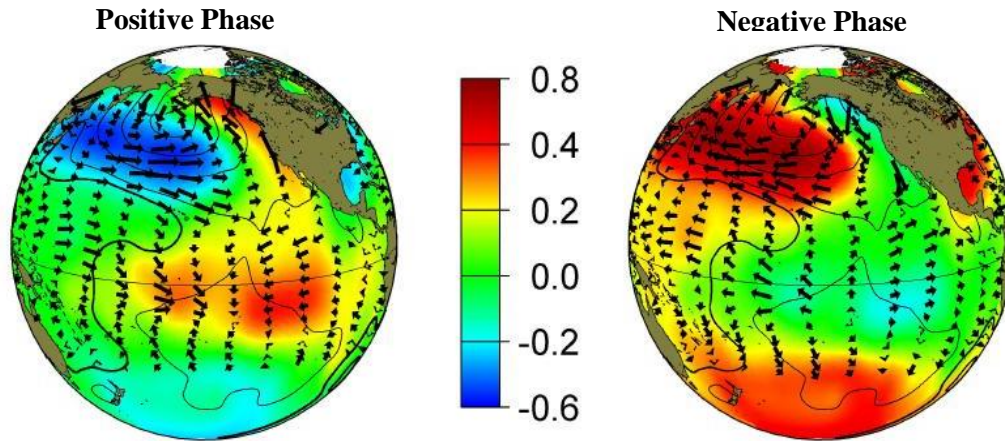


Figure 7: Sea surface temperature deviation in color, sea level pressures represented with contours, and surface wind stress with arrows. Adapted from [Mantua et al., 1997].

The Southern Oscillation Index quantifies the pressure differences between the low over west central Pacific Ocean (Darwin, Australia) and the high over the southeastern Pacific Ocean (Tahiti, French Polynesia). The change in the westward pressure gradient between these locations occurs as the equatorial Pacific sea surface becomes warmer or colder than normal. The SOI pressure fluctuations, similar to the NAO, result from anomalous SST changes in the central Pacific that strengthen and weaken the southern Hadley cell and alters the westward pressure gradient [Bjerknes, 1969]. The Niño 3.4 index measures the SST changes that occur in the Pacific from 5°N-5°S and 170°W-120°W as outlined in Figure 8.

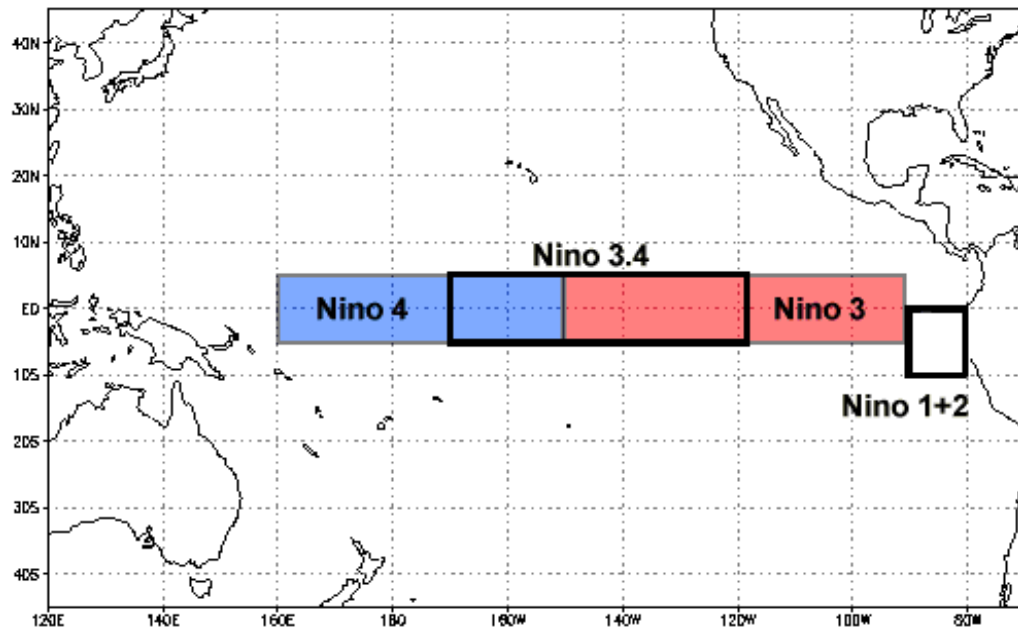


Figure 8: Regions of averaged sea surface temperature to evaluate ENSO conditions.

Provided from [NOAA, 2017].

El Niño and La Niña conditions are determined by a departure of 0.5°C (Mar-Jun) and 1.5°C (Jun-Feb), are highly correlated to the SOI. These El Niño and La Niña events occur irregularly lasting typically several month with a period of 2-7 years [Hamlet and Lettenmaier, 2000]. Merging the Southern Oscillation and Niño 3.4 index creates the bivariate El Niño Southern Oscillation (ENSO) by having their respective climatological means removed and their respective monthly values averaged against each other [Smith and Sardeshmukh, 2000]. The strongest El Niño event on record has just completed in winter 2015, surpassing the past largest departure which occurred winter of 1997 [Jacox et al., 2016]. El Niño events result in a strengthened low-latitude westerly flow crossing North America which results in increases of frontal activity. A southward displacement of the westerly jet stream (Figure 9) also develops resulting in an increased moisture flux across the southern part of North America [Kahya and Dracup, 1994]. La Niña events

generate the opposite condition with a northward deflection of the westerly jet stream and a general decrease in winter moisture flux across southern North America and Texas.

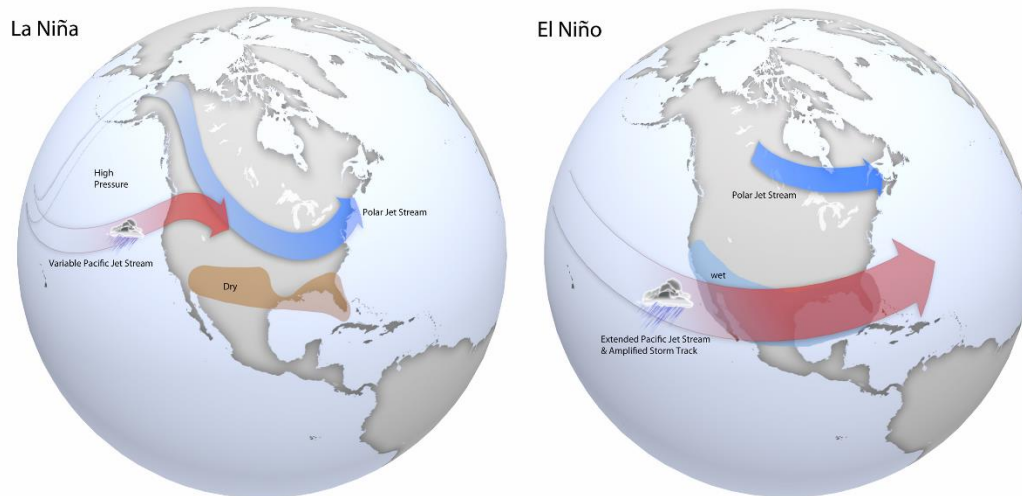


Figure 9: North American climate patterns during La Niña and El Niño conditions.

Provided from [NOAA, 2016].

3.1.2 Climate Index Datasets

All global climate indices utilized in this study were acquired from the National Oceanic and Atmospheric Administration (NOAA) data sets (see <http://www.esrl.noaa.gov/psd/data/climateindices/list/>). The AMO was created from the monthly updated SST dataset with an area weighted average over the North Atlantic from 0° to 70° N and detrended to remove any global warming trend [Enfield, 2001]. The NAO was produced from the normalized pressure difference between a station on Azores and Iceland [Hurrell, 1995]. The PDO originated from the leading principle component of SST north of 20°N in the Pacific and detrended from the global average [Zhang *et al.*, 1997]. The SOI data set utilized the standardized Tahiti pressure value minus the standardized Darwin value normalized by the monthly standard deviation. The Niño 3.4 index is

computed as the area weighted average of the sea surface temperature of 5°N-5°S and 170°W-120°W. The bivariate El Niño Southern Oscillation index (ENSO) is formed from averaging both the SOI and the Niño 3.4 values together after removing the global trend and standardizing the data [Smith and Sardeshmukh, 2000]. In the identification of El Niño and La Niña events a 20% threshold in regards to the strength of the bivariate El Niño Southern Oscillation was chosen, which is seen as a stringent definition of El/La Niño/a events. The AMO, PDO, and ENSO data sets range from 1915-2015 for the purpose of this study, while the NAO dataset was limited to 1960-2015 due to data collection starting in 1960.

3.2 Conditional Ensemble Streamflow Prediction

3.2.1 North Central Texas Regional Climate Anomalies

The temperature and precipitation dataset from the Dallas-Fort Worth region was collected from the National Weather Service historical record [NWS, 2015]. It is noted that the collection location of Dallas-Fort Worth temperature and precipitation data changed over the time series of collection (Figure 10 and Table 1). Daily mean areal precipitation (MAP) records were analyzed from the following United States Geologic Survey (USGS) reservoir monitoring stations in the upper Trinity Basin: Jacksboro station (ID: JAKT2) and Dallas station (ID: DALT2) as seen in Table 1. MAP dataset was recorded at both stations 4 times daily in accumulated inches (1 in = 25.4 mm) and ran from 1960-2015. Gaps in data collection for a time series resulted in the exclusion of that month's data from all compared data sets. The daily MAP dataset was then converted to a monthly dataset through summation of the daily precipitation totals.

The regional temperature, precipitation, and reservoir MAP datasets were transformed into climate anomalies representing deviations of temperature, precipitation and reservoir MAP from their mean regional states. These regional climate anomalies were then utilized in correlations with the global climate indices, as well as deconstructed with singular spectrum analysis in exploration of potential teleconnections.

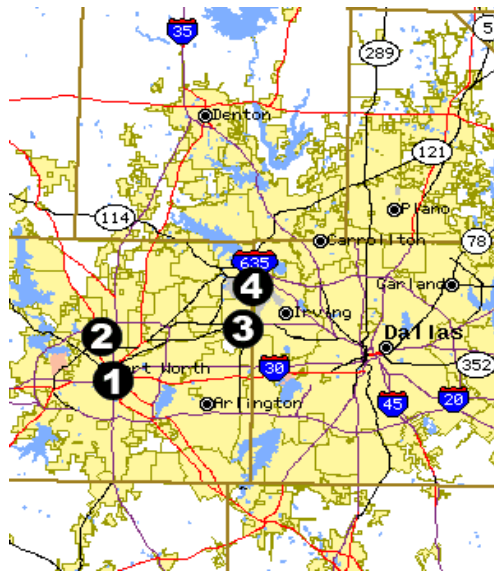


Figure 10: Map of the locations of the KDFW stations operated by the National Weather Service from 1898 to present.

1) Downtown Fort Worth 1898-1940, 2) Fort Worth Meacham Field: 1940-1953, 3) Greater Southwest International Airport: 1954-1974, 4) DFW International Airport: 1974 – present. Obtained from [NWS, 2015].

Station ID	Location Description	Station Operator	Latitude	Longitude	Total Area (km ²)	Mean Elevation (m)	Data Collected	Date of Collection
SGET2	Clear Creek near Sanger	USGS	33° 20' 06.00" N	097° 10' 38.99" W	763.88	277.68	Mean Areal Precipitation	1959 - Present
DCJT2	Denton Creek near Justin	USGS	33° 07' 21.00" N	097° 17' 24.00" W	1040.94	282.30	Mean Areal Precipitation	1959 - Present
GLLT2	Elm Fork Trinity River at Gainesville	USGS	33° 37' 21.00" N	097° 09' 09.00" W	441.96	299.11	Mean Areal Precipitation	1959 - Present
JAKT2	West Fork Trinity River near Jacksboro	USGS	33° 17' 50.99" N	098° 04' 39.00" W	1767.17	333.04	Mean Areal Precipitation	1959 - Present
BRPT2	Big Sandy Creek near Bridgeport	USGS	33° 13' 50.99" N	097° 41' 23.99" W	883.97	294.94	Mean Areal Precipitation	1959 - Present
BPRT2	West Fork Trinity River at Bridgeport Reservoir	USGS	33° 13' 20.99" N	097° 49' 53.99" W	2879.10	312.77	Mean Areal Precipitation	1959 - Present
BOYT2	West Fork Trinity River near Boyd	USGS	33° 05' 06.00" N	097° 33' 23.99" W	4490.91	260.11	Mean Areal Precipitation	1959 - Present
EAMT2	West Fork Trinity River at Eagle Mountain Reservoir	USGS	32° 52' 05.99" N	097° 27' 38.99" W	5134.12	248.57	Mean Areal Precipitation	1959 - Present
FLWT2	West Fork Trinity River at Lake Worth	USGS	32° 47' 35.99" N	097° 24' 23.99" W	5396.04	238.21	Mean Areal Precipitation	1959 - Present
LWFT2	Clear Fork Trinity at Lake Weatherford	USGS	32° 46' 21.00" N	097° 40' 08.99" W	271.62	337.30	Mean Areal Precipitation	1959 - Present
ADOT2	Clear Fork Trinity River near Aledo	USGS	32° 38' 35.99" N	097° 33' 38.99" W	641.30	309.66	Mean Areal Precipitation	1959 - Present
BNBT2	Clear Fork Trinity River at Benbrook Lake	USGS	32° 39' 20.99" N	097° 26' 38.99" W	1106.22	271.26	Mean Areal Precipitation	1959 - Present
LART2	Village Creek at Lake Arlington	USGS	32° 43' 05.99" N	097° 11' 08.99" W	379.97	218.27	Mean Areal Precipitation	1959 - Present
BDWT2	Waxahachie Creek at Bardwell Lake	USGS	32° 15' 05.99" N	096° 38' 24.00" W	459.23	180.76	Mean Areal Precipitation	1959 - Present
DAWT2	Richland Creek at Navarro Mills Lake	USGS	31° 57' 05.99" N	096° 41' 38.99" W	874.16	177.88	Mean Areal Precipitation	1959 - Present
RCET2	Chambers Creek near Rice	USGS	32° 12' 06.00" N	096° 31' 09.00" W	2146.18	157.71	Mean Areal Precipitation	1959 - Present
FFLT2	Richland Creek at Richland-Chambers Reservoir	USGS	31° 57' 50.99" N	096° 08' 38.99" W	5078.09	115.00	Mean Areal Precipitation	1959 - Present
TRNT2	Cedar Creek at Cedar Creek Reservoir	USGS	32° 10' 35.99" N	096° 03' 53.99" W	2679.90	123.11	Mean Areal Precipitation	1959 - Present
KDFW	Dallas Fort Worth International Airport	NWS	32° 53' 49.00" N	97° 02' 17.00" W	N/A	164.99	Precipitation & Temperature	1974 - Present
	Greater Southwest International Airport	NWS	32° 49' 53.00" N	97° 02' 57.00" W	N/A	N/A		1954 - 1974
	Fort Worth Meacham Field	NWS	32° 49' 13.00" N	97° 21' 35.00" W	N/A	N/A		1940 - 1954
	Downtown Fort Worth	NWS	32° 45' 26.49" N	97° 19' 59.45" W	N/A	N/A		1898 - 1940

Table 1: Data collection stations provided and operated by the United States Geologic Survey and the National Weather Services for the Trinity River Basin. Station coordinates, area coverage, elevation, date of data collection, and type of data collection are provided in table.

The study also incorporated the gridded Livneh Contiguous United States (CONUS) near-surface meteorological dataset from 1915-2012 for reconstructing reservoir catchment meteorology [Livneh *et al.*, 2013]. This dataset contained temperature (minimum and maximum), precipitation, and wind speed on a $1/16^\circ$ by $1/16^\circ$ resolution calculated from 20,000 National Climate Data Center (NCDC) station inputs across the US domain. In addition, hydrometeorological variables such as evaporation flux, generated from the original data meteorological dataset using the Variable Infiltration Capacity (VIC) hydrologic model (version 4.1.2.c), were included. These datasets were then applied to construct individual variable time series for each reservoir station hydraulic catchment by averaging the variable grid values contained in each hydraulic catchment. The reservoir MAP data only extended back to 1960, a time interval too short to be compared with global climate indices that have a periodicity of 50-70 years. Thus, it was necessary to artificially extend monthly reservoir precipitation, through the use of the Livneh datasets, to identify potential teleconnections between the global and regional climate pattern.

The Livneh CONUS reservoir precipitation datasets were then utilized in the creation of cumulative distribution functions and probability density functions in regards to AMO phases, PDO phases, and El Niño and La Niña events in order to determine changes in regional precipitation distributions.

3.2.2 Computation of Climate Anomalies and Normalization

The monthly averaged and standardized areal anomalies (x'_i) for temperature and precipitation for the stations (section 3.1) were calculated by subtracting the mean (\bar{x}) over

the period 1900-2015 (for decadal variations) and 1960-2015 (for inter-annual variations) from the observed values (x_i) (Eq. 1) :

$$x'_i = x_i - \bar{x} \quad (1)$$

with

$$\bar{x} = \left(\frac{1}{n} * \sum_{j=1}^n x_j \right) \quad (2)$$

The monthly averaged observed temperature and precipitation anomalies x'_i were then used to compute the normalized distribution $\phi(x)$ with a standard deviation of 1 and a mean of 0 for statistical analysis (Eq. 3):

$$\phi(x) = \sqrt{\frac{\sum (x'_i)^2}{n-1}} \quad (3)$$

The distribution analysis (Eq. 3) was preformed to accurately compute trends when implementing higher order statistical analysis such as singular spectrum analysis.

3.2.3 Moving Average Filter

A moving average filter was applied to the regional climate anomaly and global climate indices before correlations were taken. The moving average filter (Eq. 4) is shown with the weighted value (Eq. 5) for the filtered data. In equation 4, m_t denotes the filtered data, k is the length of filter, a_j is the filter weight, and x_t denotes the input data at time t . A value of k was chosen to be 2 for the monthly average filter [Booth *et al.*, 2006].

$$m_t = \left(\sum_{j=-k}^k a_j x_{t-j} \right) \quad (4)$$

with

$$a_j = \frac{1}{2k+1} \quad (5)$$

3.2.4 Blackman-Turkey Spectrum Analysis

A spectrum analysis was performed on the datasets to determine at which period(s) the most prominent oscillation components were present. This process involves the use of a Fast Fourier Transform (FFT; Eq. 6) to transform the data from a time domain into a frequency domain with X_k representing the FFT output. The Blackman-Turkey method utilizes an autocorrelation function (r_k) to smooth the wave, as well as a windowing effect (w_k). Combining these elements creates the structure of the Blackman-Turkey Algorithm (Eq. 7), where k equals lag and N is maximum lag [Blackman and Tukey, 1958; Percival and Walden., 1993].

$$X_k = \sum_{n=0}^{N-1} x_n e^{-i2\pi k \frac{n}{N}} ; k = 0, \dots, N - 1 \quad (6)$$

$$X_k(f) = \sum_{k=0}^{N-1} w_k r_k e^{-i2\pi k f} \quad (7)$$

3.2.5 Correlations and Cross-Correlations

Linear correlation coefficient (R) between two datasets was obtained by using the Pearson product-moment linear correlation method (Eq. 8) with \bar{x} and \bar{y} representing the mean value of the datasets. The Pearson coefficient of determination (R^2) was also calculated through squaring the Pearson product linear correlation coefficient.

$$R = \frac{\sum_{i=1}^n (x_i - \bar{x})(y_i - \bar{y})}{\sqrt{\sum_{i=1}^n (x_i - \bar{x})^2} \sqrt{\sum_{i=1}^n (y_i - \bar{y})^2}} \quad (8)$$

The cross-correlation function (CCF) equation (Eq. 9) introduces a lag time τ into the Pearson equation (Eq. 8) so that the change in the Pearson product is determined in response to the offset of data points enabling the determination of delayed forcing in the

climate system in reference to our regional parameters, such as temperature and precipitation anomalies [Zwiers and Storch, 1999].

$$CCF_{xy} = \frac{\sum_{i=1}^n (x_i - \bar{x})(y_{i-\tau} - \bar{y})}{\sqrt{\sum_{i=1}^n (x_i - \bar{x})^2} \sqrt{\sum_{i=1}^n (y_{i-\tau} - \bar{y})^2}} \quad (9)$$

3.2.6 Empirical Cumulative Distribution and Probability Density Function

The empirical cumulative distribution function for the regional precipitation was generated by taking each reservoir's monthly precipitation value for all months within the selected climate phase and inputting them into an empirical cumulative distribution function (Eq. 10). The discrete probability density function (Eq. 11) is generated based on the probability of an observed outcome occurring. Its integral generates the cumulative distribution function.

$$F_X(x) = \int_{-\infty}^x f(x) dt \quad (10)$$

$$f(x) = \frac{1}{n} \sum_{i=1}^n K_h(x - x_i) \quad (11)$$

3.3 Hydrometeorological Forecasting

The Livneh CONUS near surface meteorological conditions, introduced in section 3.2.1, dataset from 1915-2012 that was reconstructed into TRWD individual reservoir catchment datasets was employed in this half of the study. It was utilized in the calculation of the Potential Evapotranspiration (PET) and the Standardized Precipitation Evapotranspiration Index (SPEI). In addition, the Livneh CONUS reconstructed dataset was provided as regional climatology inputs for the artificial neural network model.

3.3.1 Potential Evapotranspiration

Calculating potential evapotranspiration is necessary for the construction of regional drought indices, which rely on the calculated flux of regional soil moisture. Potential evapotranspiration (PET), also referred to as reference evapotranspiration, is the maximum potential amount of evapotranspiration that would occur with ample amounts of water present. PET values can be derived from the application of Penman's equation (Eq. 12) which involves computation of the atmospheric (E_{aero}) and radiative (E_{rad}) components of radiation by

$$E_{Pen} = E_{rad} + E_{aero} = \frac{\Delta}{\Delta + \gamma} * \frac{(R_n)}{\gamma} + \frac{\gamma}{\Delta + \gamma} * \frac{6.43(f_U)D}{\lambda} \quad (12)$$

Equation (12) is parameterized by the slope of saturation vapor pressure curve (Δ) in (kPa/°C), the net surface radiation (R_n) in (MJ/m²/d), the psychrometric coefficient (γ) in (kPa/°C), the Penman wind function (f_U), the vapor pressure deficit (D), and the latent heat of vaporization (λ) in (MJ/kg) [Penman, 1948].

It should be noted that Eq. (12) requires an intensive dataset including temperature, relative humidity, wind speed, extra-terrestrial radiative forcing, and surface radiative forcing. These variables are not present across this study's 97-year time series, so a modified approximation of the Penman equation is necessary. The modified Hargreaves method, developed for use with limited datasets, is described by

$$PET \approx 0.0013 * 0.408R_a * (T_{avg} + 17) * (TD - 0.0123P)^{0.76} \quad (13)$$

and is computed from incoming downward solar radiation R_a in ($\text{MJ m}^{-2}\text{d}^{-1}$ or $86.4 \cdot 10^{-3} \text{ W m}^{-2}$), average temperature (T_{avg}) in ($^{\circ}\text{C}$), temperature range (TD) in ($^{\circ}\text{C}$), and precipitation (P) in (mm/month) [Droogers and Allen, 2002]. The Hargreaves method while requiring less data atmospheric data still computes PET within 97-101% of a measured lysimeter, a measuring device that can measure evapotranspiration [Beguería et al., 2014].

3.3.2 Standardized Precipitation Evapotranspiration Index

The standardized precipitation evapotranspiration index (SPEI) was developed as a combination of the standard precipitation (SPI) and Palmer drought severity index (PDSI) [Vicente-Serrano et al., 2010]. The SPI was a multi-scalar precipitation index that lacked the incorporation of evapotranspiration data while the PDSI was a measure of soil moisture evapotranspiration that could only be viewed in one timescale, which varies but is typically on the annual scale. The SPEI merged these two concepts to generate a drought index utilizing evapotranspiration that functions in a multi-scalar nature so that different drought types could be characterized [Vicente-Serrano et al., 2010]. The SPEI is constructed by calculating the difference between precipitation (P) and reference evapotranspiration (PET), or

$$SPEI = P - PET \quad (14)$$

Computation of SPEI can be obtained by a standardized (mean=0 and standard deviation SD = 1) probability distribution function $F(D)$, given by

$$F(D) = \left[1 + \left(\frac{\alpha}{D - \gamma} \right)^{\beta} \right]^{-1} \quad (15)$$

as a function of a log-logistic distribution of the difference of P minus PET (D) with scale (α), shape (β), and location parameter (γ) [Beguería *et al.*, 2014].

Figure 11 shows the calculated SPEI values on the reservoir SGET2 surface for a 3 month, 6 month, and 12 month time step. As can be seen, the 12 month SPEI has the least noise and most closely resembles the PDSI while the 3 month SPEI more closely resembles a precipitation anomaly time series. For the purpose of this study, a 6 month SPEI was chosen in determining the hydrometeorological conditions as it has been shown to correlate with soil moisture, precipitation, and streamflow [Vicente-Serrano *et al.*, 2010; Wolf, 2012; Wu *et al.*, 2016].

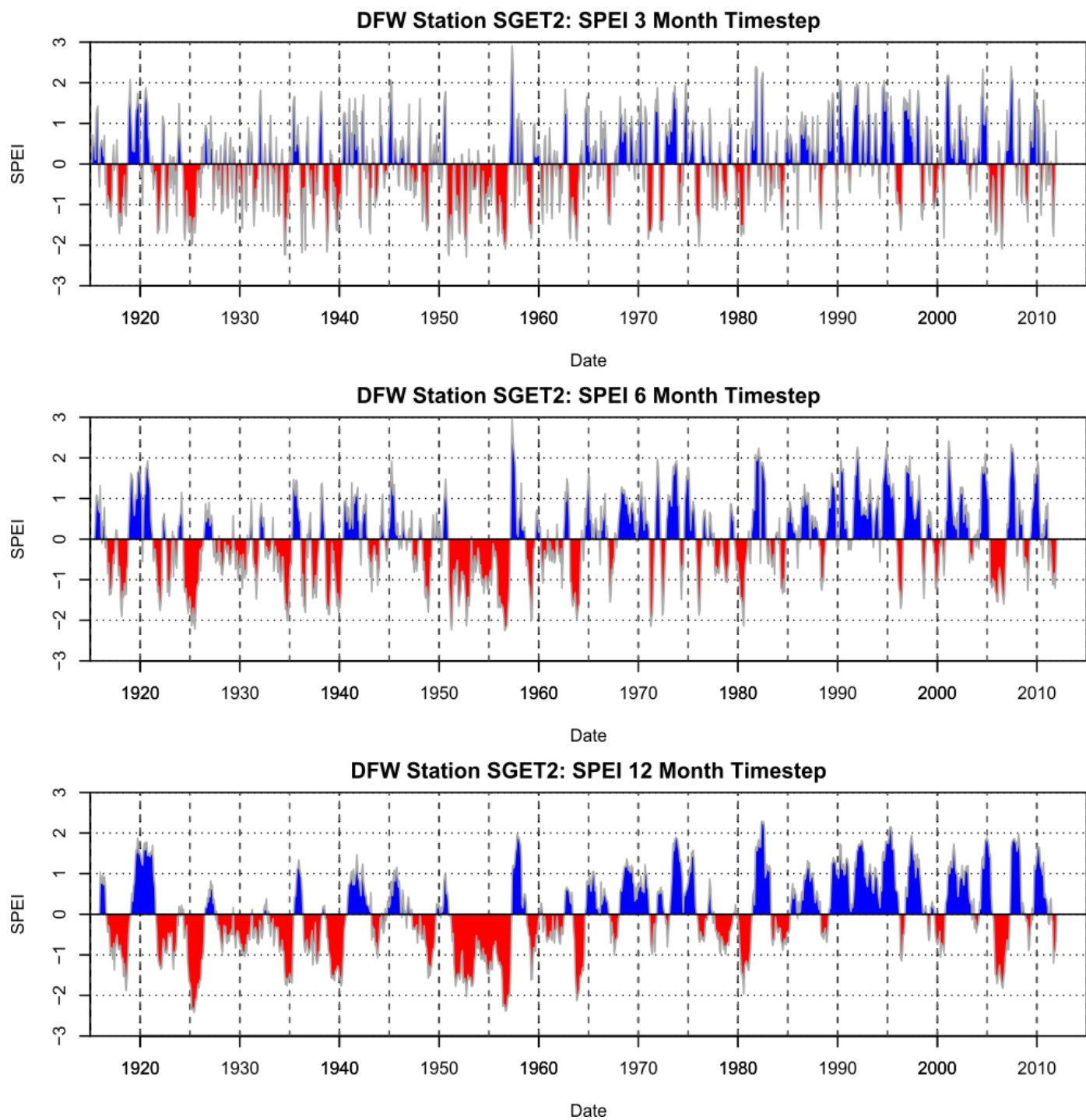


Figure 11: Time series of the standardized precipitation evapotranspiration index (SPEI) for reservoir catchment SGET2 and for time steps 3, 6, and 12 months.

3.4 Artificial Neural Network (ANN) Model

Artificial Neural Network modeling was utilized in this study as a means of forecasting future reservoir hydrometeorological conditions through a machine learning algorithm. The introduction section of this chapter explains the development, benefits, and limitations of Artificial Neural Network modeling, while the model description section explains the exact configuration and parameters of the model used in this study.

3.4.1 Introduction

Artificial Neural Networks (ANN) were first developed by replicating the structure and process of how the mammal neurologic brain functions [Basheer and Hajmeer, 2000]. As seen in Figure 12, a mammal's neuron receives data from multiple inputs through dendrites where the information is subsequently processed through the soma and an output is sent through the corresponding axon to synapses connected to other neurons. On a much smaller scale this is the basic structure of an ANN model and how it processes input and output data. An ANN model must at least consist of three layers: an input, hidden neuron, and output layer. Input data is processed through a hidden neuron layer that utilizes a chosen training algorithm and back propagating error to adjust the hidden neuron's weights to match the training output sequence [Flood and Kartam, 1994]. By training the model based on output error, relationships are derived between the input variables and the output variable, and reflected in the training of the hidden neuron weights, as inputs shown to give better predictions of the output increase the hidden neuron weights.

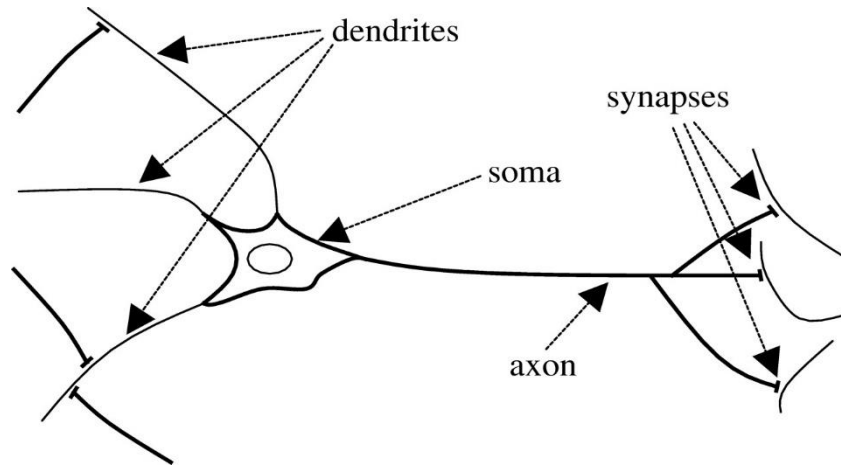


Figure 12: The structure of a mammalian neuron. Adapted from [Furber and Temple, 2007].

ANN models are proven to be robust at extracting patterns from noisy data as well as being capable of deriving non-linear relationships between data inputs and outputs. Making ANN models ideal for drought forecasting, which exhibits non-linear relationships between meteorological parameters that contain a low signal to noise ratio. ANN models also only require knowledge of the central factors that influence the studied process, not a derived relationship of the process being examined [Baawain *et al.*, 2005]. An important qualification, as determination of future drought patterns based on present day meteorological parameters has not yet been dynamically quantified by climate modelling.

3.4.2 Model Description

The ANN model utilized in this study is classified as a feed-forward multi-perceptron model with back propagating error [Hornik *et al.*, 1989]. As shown in Figure 14, up to 10 data inputs were used with the model and separated into the following groups for this study; climate indices (AMO, PDO, ENSO), evaporation variables (evaporation,

potential evapotranspiration, wind speed), precipitation, temperature extremes, and the SPEI value. Climate indices, like AMO, PDO, and ENSO, were selected as they showed signs of potential teleconnections during earlier correlations and contained the necessary data values for the length of the modeling (1915-2012).

An architecture of four hidden neurons was chosen after varying the number of hidden neurons showed four hidden neurons providing the lowest amount of error, as seen in Figure 13. The ANN model was then trained with 70% (or 68 years) of the dataset range from (1915-1983) and tested against 30 percent (29 years) of the data range (1983-2012). The data output was varied depending on forecast length, e.g. to generate a model forecast for 2 months lead time the data output would be trained utilizing SPEI values 2 months ahead of the data input. Utilizing the above process reduces the overall forecasting error with longer lead times as the error generated from previous predictions does not cumulate since different models are implemented for separate lead times. This methodology differs from the alternative classical approach which would incorporate the use of the SPEI drought indices natural autocorrelation to determine future SPEI values based on multiple previous SPEI values [Özger *et al.*, 2012]. This study does not utilize the SPEI autocorrelation relationship in forecast prediction as it would disrupt the ranking of the regional climatology and global climate indices in terms of forecast importance in predicting SPEI values, and it would propagate forecast error across forecasted months, for example a 2 month ahead prediction would contain the error from the 1 month prediction.

The overall forecasting ability of the ANN model was quantified with the Brier skill score against climatology (Eq. 16) [Hamill and Juras, 2006]. The Brier skill score is computed as the ability of the forecast model to better determine predicted values than the general variability of the forecasted system. As the model's mean square error approaches that of the SPEI variability the model skill score falls to 0 representing no forecasting ability

in reference against the natural climatology of the regional SPEI values. The regional climatology for this study was determined from the testing data range of 1983-2012. Model skill would be expected to increase if the regional climatology was taken from the total dataset 1915-2012. Therefore, it can be considered that this model's skill scores are a conservative estimation.

$$\text{Brier Skill Score} = 1 - \frac{MSE}{Var(SPEI)} \quad (16)$$

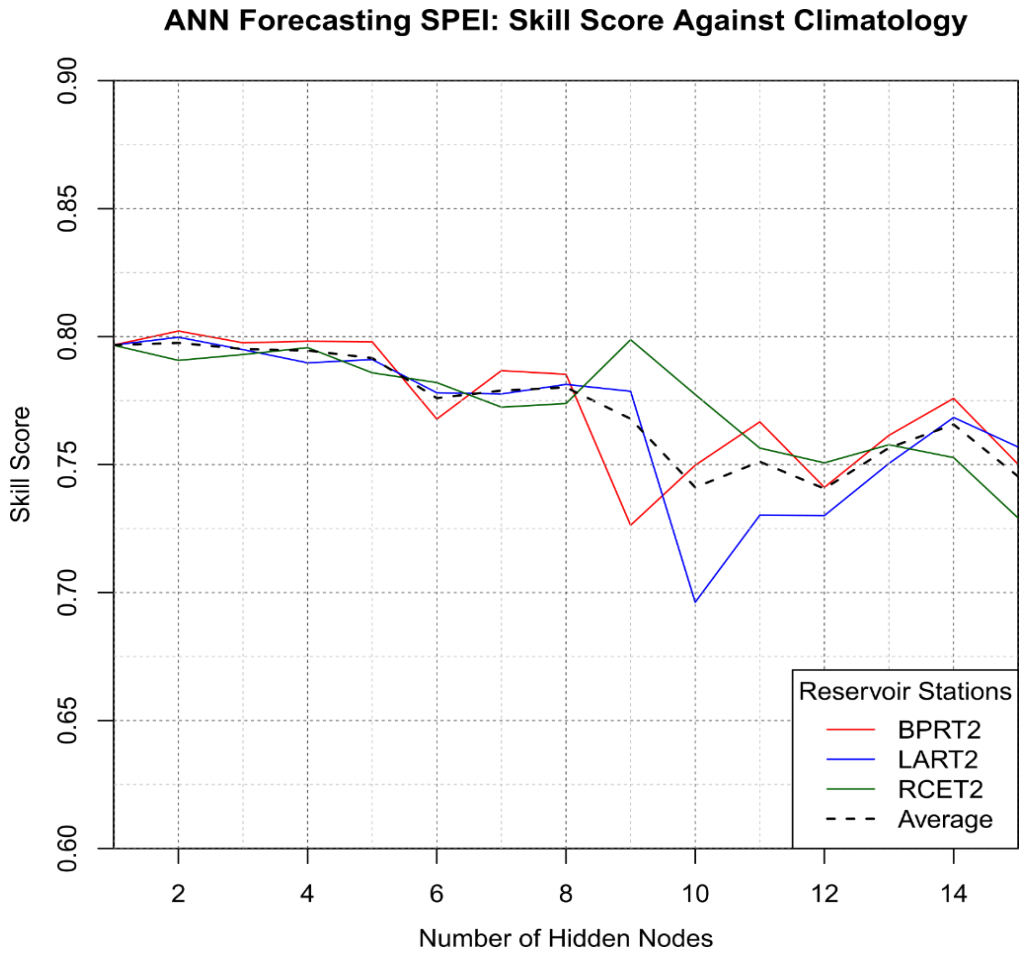


Figure 13: Artificial neural model forecasting skill in relation to the variation of the number of hidden neurons. Optimum architecture identified as 4 hidden neurons.

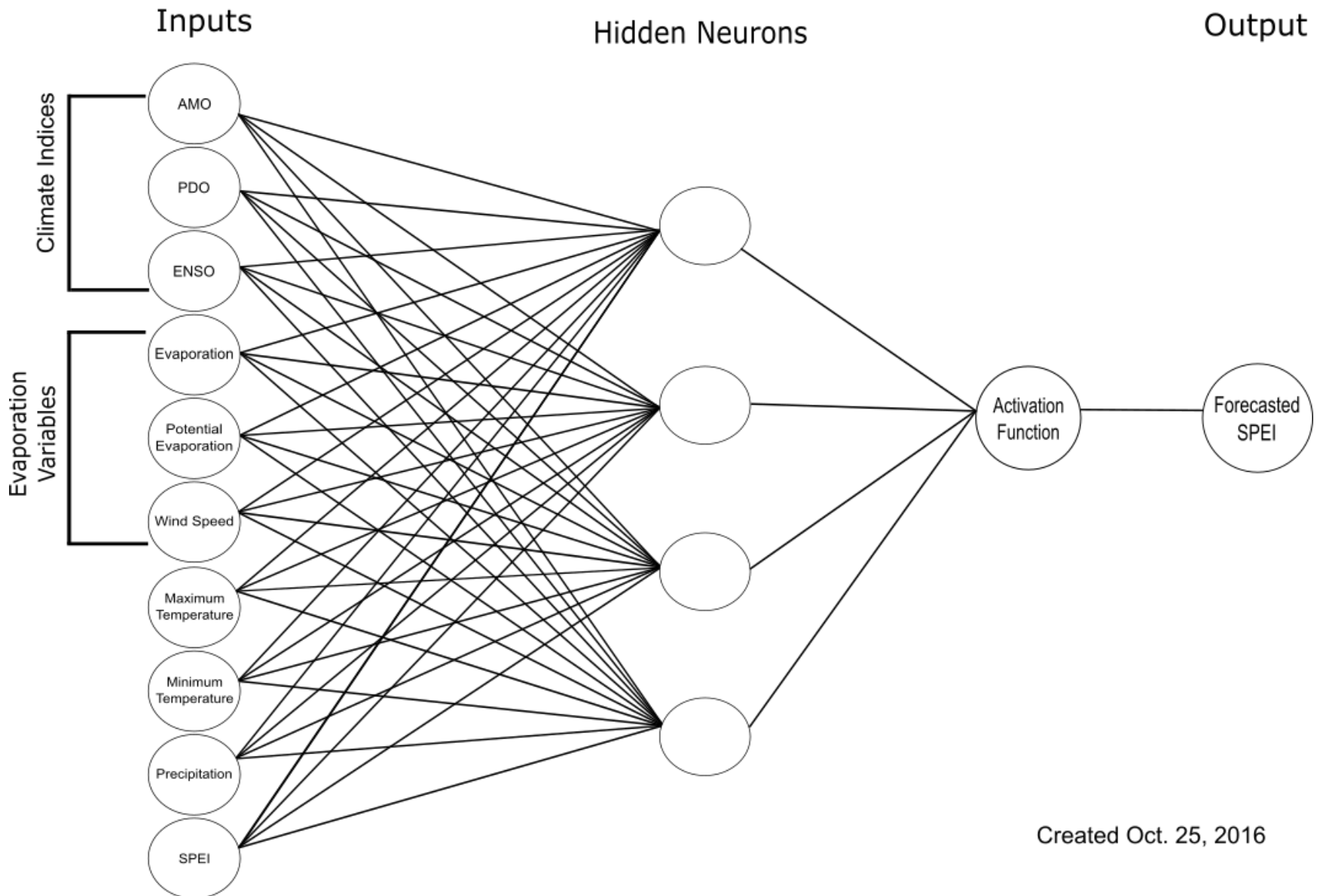


Figure 14: Artificial neural network model architecture with a gaussian symmetric activation function. Model inputs were varied to determine input importance in forecasting for climate indices, evaporation variables, temperature, and precipitation.

Chapter 4

Conditional Ensemble Streamflow Prediction

4.1 Results

4.1.1 Regional Climate Anomalies and Global Climate Indices Correlations

A Pearson-correlation test was implemented in matrix form on the climate indices' datasets for months indicative of La Niña or El Niño conditions. El Niño conditions are classified with the number 1 and La Niña defined with number -1 when the monthly bivariate El Niño Southern Oscillation Index is above the 20th percentile, whereas all other months are classified with the number 0. All datasets used in these linear correlations (Eq. 8) were smoothed with a 5-month moving average filter (Eq. 4). A significance test was also performed with correlation coefficient results passing a 95% (p-value < 0.05) confidence level highlighted in red. The correlation matrix in Figure 15 and Table 2 show the relation between climate indices and months pertaining to El Niño conditions. During El Niño events, the mean areal precipitation from Station JAKT2 does correlate moderately with the index PDO index ($R= 0.57$) and has a low correlation with the other climate indices (NAO ($R=0.31$), AMO ($R=-0.31$), and SOI ($R=-0.35$)). However, the Pearson correlation coefficient between Dallas Fort Worth (DFW) Airport precipitation values and climate indices appears to be negligible. In contrast during La Niña events, the correlation coefficient between the regional precipitation anomaly from the DFW Airport and climate indices is higher (e.g. for the AMO and SOI indices ($R=0.31$ and $R=-0.52$ respectively)) (Figure 16, Table 2). There is a low correlation for the PDO index ($R=-0.31$) climate, in regards to the JAKT2 station precipitation data. The correlations that pass the significance test range from negative moderate ($R=-0.52$) to positive low ($R=0.31$). The low values

above may be linked to noise or higher frequency oscillations in the signal which limit the precision of the Pearson linear correlation coefficient.

4.1.2 Spectral Analysis

A Fourier spectrum analysis (Eq. 6) was implemented on the climate indices datasets from 1900-2015 to determine the frequencies and periods with the largest oscillation power. The Blackman-Turkey method (Eq. 7) was utilized with a 650-bin discrete Fourier transform window for all climate datasets except the ENSO dataset, for which a 126-bin discrete Fourier transform window was applied. Figure 17(A) shows the AMO power spectrum peak at a value in the range of 0.0012-0.0016, this coincides with a period of 52- 70 years, which is supported by the literature for the AMO [Enfield, 2001]. The PDO, Figure 17(B), power spectrum peak ranges from 49 years to 55.5 years and 5.5 years and 6 years respectively. The DFW precipitation anomaly, Figure 17(C), has multiple low frequency peaks at 2.9 years, 4.1 years, 8.3 years, and 13.8 years; an indication that multiple signals with differing periods are likely attributing to the variability in the DFW precipitation anomaly. The ENSO index, Figure 17(D), has two main peaks one at 5.2 years and the other at 2.31 years. The largest power spectrum for the DFW temperature anomaly, Figure 17(E), has a period of 52 years and coincides with the period of the AMO. The interpretation of spectral analysis utilizing the fast Fourier function is limited to a maximum period length of 57.5 years, as the function can only represent periods up to half the length of available data used, which is 115 years for this study. As the AMO, PDO, and DFW temperature anomaly contain periodicities close to the maximum lower frequencies visible, our datasets may contain lower frequency oscillations that we are currently unable to properly quantify yet.

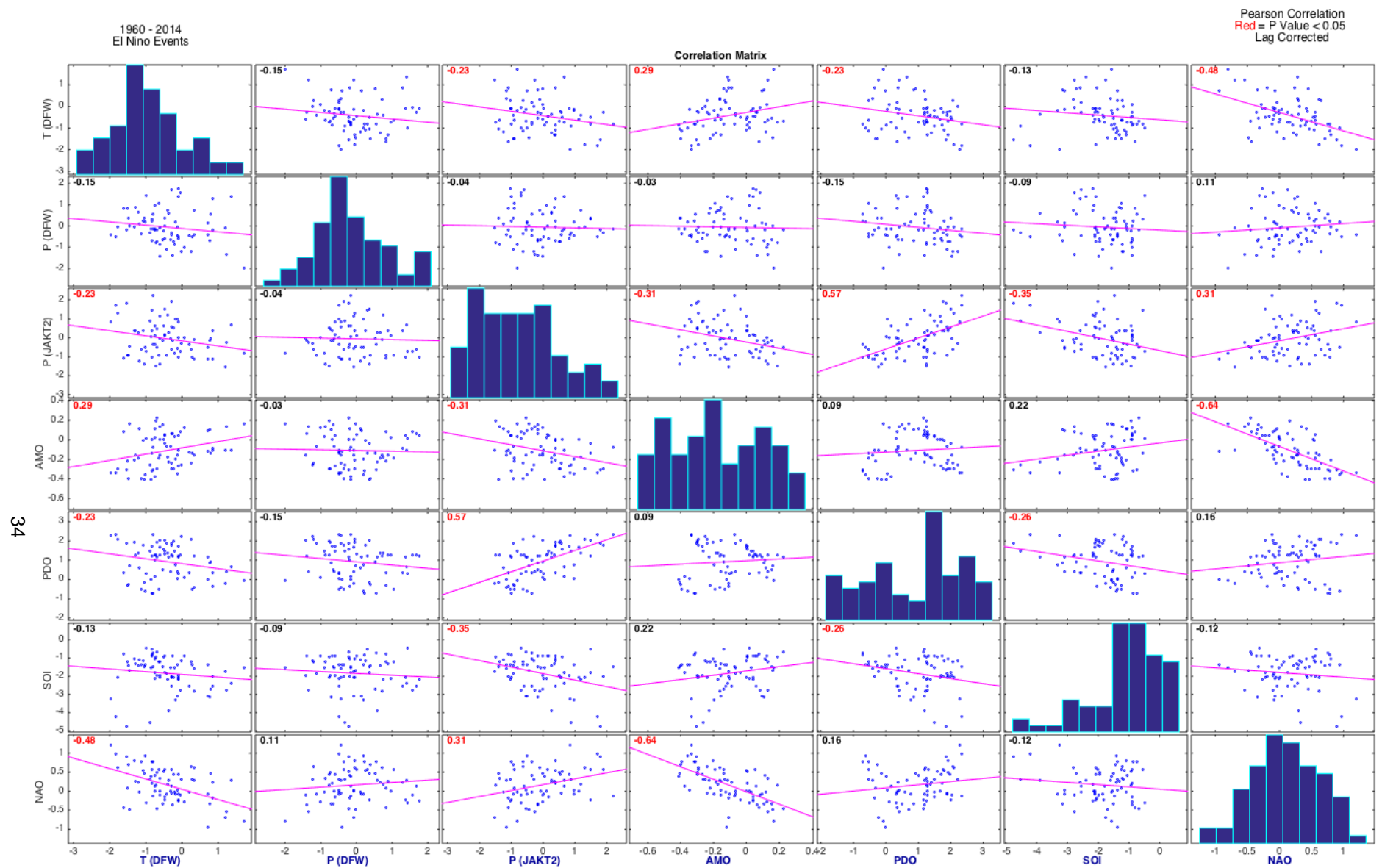


Figure 15: Pearson correlation between temperature anomaly (T) and precipitation anomaly (P) of stations in North Central Texas (Dallas Fort Worth Airport, DFW, and WF Trinity R NR Jacksboro station, JAKT2) and major climate indices (AMO, PDO, SOI, NAO) during El Niño climate conditions, along with a representative histogram of each correlated variable.

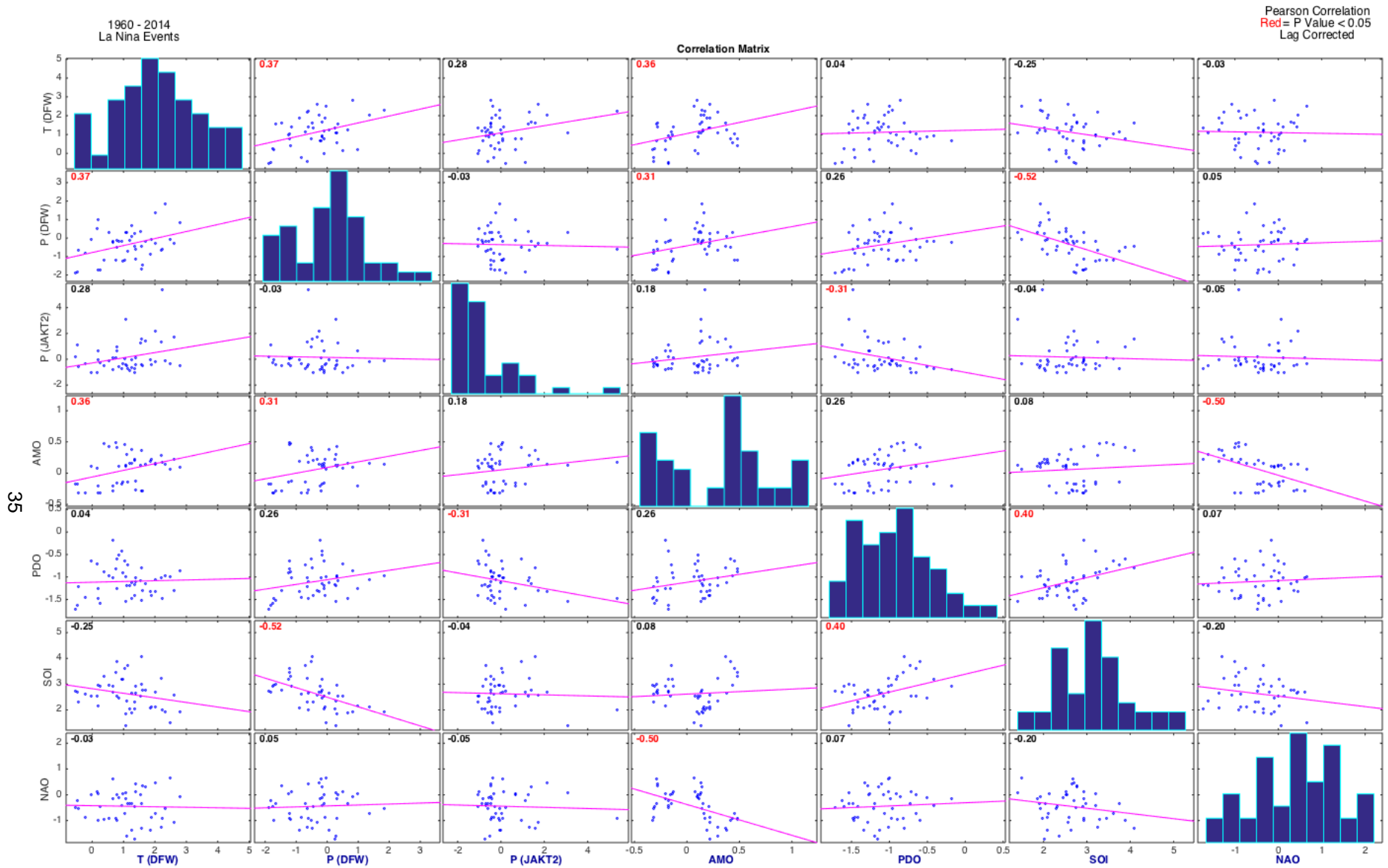


Figure 16: Pearson correlation between temperature anomaly (T) and precipitation anomaly (P) of stations in North Central Texas (Dallas Fort Worth Airport, DFW, and WF Trinity R NR Jacksboro station, JAKT2) and major climate indices (AMO, PDO, SOI, NAO) during La Niña climate conditions, along with a representative histogram of each correlated variable.

El Niño Conditions (1960-2014)	Pearson Correlation- (R)	Significance Test	La Niña Conditions (1960-2014)	Pearson Correlation- (R)	Significance Test
AMO & T(DFW)	0.29	< 0.05	AMO & T(DFW)	0.36	< 0.05
PDO & T(DFW)	-0.23	< 0.05	PDO & T(DFW)	0.04	> 0.05
SOI & T(DFW)	-0.13	> 0.05	SOI & T(DFW)	-0.25	> 0.05
NAO & T(DFW)	-0.40	< 0.05	NAO & T(DFW)	-0.03	> 0.05
AMO & P(DFW)	-0.03	> 0.05	AMO & P(DFW)	0.31	< 0.05
PDO & P(DFW)	-0.15	> 0.05	PDO & P(DFW)	0.26	> 0.05
SOI & P(DFW)	-0.09	> 0.05	SOI & P(DFW)	-0.52	< 0.05
NAO & P(DFW)	0.11	> 0.05	NAO & P(DFW)	0.05	> 0.05
AMO & P(JAKT2)	-0.31	< 0.05	AMO & P(JAKT2)	0.18	> 0.05
PDO & P(JAKT2)	0.57	< 0.05	PDO & P(JAKT2)	-0.31	< 0.05
SOI & P(JAKT2)	-0.35	< 0.05	SOI & P(JAKT2)	-0.04	> 0.05
NAO & P(JAKT2)	0.31	< 0.05	NAO & P(JAKT2)	-0.05	> 0.05

Table 2: Pearson correlation coefficient (R) and significance test (p-value) between temperature anomaly (T) and precipitation anomaly (P) of stations in North Central Texas (Dallas Fort Worth Airport, DFW, and WF Trinity R NR Jacksboro station, JAKT2) and major climate indices (AMO, PDO, SOI, NAO) during El Niño and La Niña climate conditions. Note that $p < 0.05$ (red) denotes statistical significance.

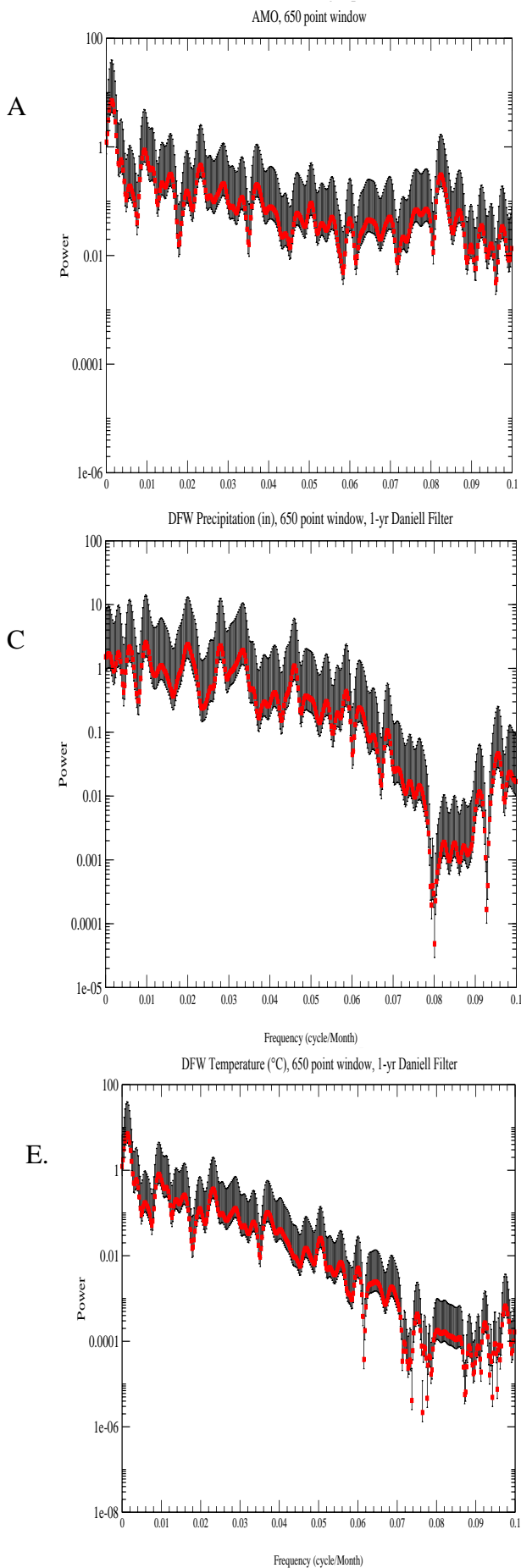


Figure 17: Singular spectrum analysis of global climate indices and regional climate anomalies: A) AMO power spectrum with a 650 discrete Fourier transform (DFT) bin window, B) PDO power spectrum with a 650 DFT bin window, C) DFW precipitation anomaly power spectrum with a 650 DFT bin window and annual moving average filter, D) ENSO power spectrum with a 126 DFT bin window, E) DFW temperature anomaly power spectrum with a 650 DFT bin window and annual moving average filter.

4.1.3 Empirical Cumulative Distribution Function and Probability Density Function

Analysis

Monthly and seasonal precipitation data for each of the reservoir catchment areas was analyzed in respect to positive and negative AMO and PDO phases as well as El Niño and La Niña events and separated in respective phases. These two datasets with positive and negative phases were then analyzed by reconstructing the cumulative distribution function and the probability density function to evaluate whether the different climatic phases generated discrimination between the two states, or whether there was an overall mean change in the precipitation probability distribution. This method was applied for annual and seasonal (with focus on winter, and spring) values of total precipitation for the Trinity River basin.

The annual total precipitation probability density and cumulative distributions for the different climate phases for our study area can be seen in Figures 18, 19, and 20. Both AMO phase's (Figure 18) and El Niño and La Niña (Figure 19) event's effect on regional annual precipitation show a discernable discrimination between phases in regards to annual precipitation, with the AMO phase having a more consistent uniform discrimination of roughly 127 mm (5 in) of annual precipitation. El Niño and La Niña events exhibit a comparable annual discrimination on regional precipitation though it is not uniform, as the La Niña probability density function (pdf) exhibits a bimodal peak. It is important to note that ENSO events are not necessarily represented by a change in annual mean precipitation as these are probabilistic plots which establish the likelihood of an ENSO event deviating from typical annual precipitation. The PDO phases (Figure 20) exhibited little to no precipitation discrimination on an annual basis with the PDO probability density phases closely matching except for a muted bimodal peak in regards to the negative PDO phase. The seasonal winter probability density and cumulative distribution functions

(Figures 21-23) display El Niño and La Niña events (Figure 22) as the prominent means of winter precipitation discrimination when compared to the AMO (Figure 21) and PDO (Figure 23). The seasonal spring probability density and cumulative distribution functions for precipitation (Figures 24-26) were also compared, as seasonal spring precipitation generates the majority of the seasonal precipitation that affects our study area's annual precipitation. The AMO phase discrimination (Figure 24) shows a consistent small discrimination of 25 mm - 50 mm (or 1 in - 2 in) for a total accumulated precipitation of 200 mm (or 8 in). El Niño and La Niña events (Figure 25) exhibit a greater discrimination of 63 mm (2.5 in), though it is not uniform and mostly generated from La Niña events exhibiting a bimodal peak. The PDO probability density and cumulative distribution (Figure 26) showed the lowest levels of precipitation discrimination, consistent with the annual and winter discrimination results.

4.2 Discussion

In summary, the Pearson correlations produced weak to moderate correlations between the AMO, ENSO, and PDO global climate indices and regional climatology, with statistical significance within the 95% confidence level. This null hypothesis significance level test is an unreliable significance metric because the global and regional climate variations are related to global external forcing, such as variations in greenhouse, solar, and aerosol forcing, and internal climate variation of the climate system [Donges *et al.*, 2009]. Accordingly, the significance test, which determines whether no relationship is present in the case of the null hypothesis should be skewed to positive results. The significance test bias is also accentuated by the large dataset correlations which would increase the likelihood of the data falling into the 95% confidence interval [Nicholls, 2001]. Thus, our analysis suggests that the Pearson correlation (Table 2) is limited to identify

climate teleconnections between the global and regional climate due to the non-linear nature of these teleconnections [Donges *et al.*, 2009; Hlinka *et al.*, 2014]. The limitations in the Pearson correlation methodology in accounting for the relationship between multi-variable, non-linear systems also reduces the ability of generating positive correlation matches between regional changes of temperature and precipitation and climate teleconnections. While overall a positive AMO phase is indicative of increased temperature and lower precipitation, this does not remain consistent when considering the additional complexity of other climatological events simultaneously occurring such as an El Niño or La Niña event.

The singular spectrum analysis was employed in determination of the overall oscillation pattern of the global climate indices and the regional climatology in terms of temperature and precipitation changes. The above approach exploits the unique oscillatory period property of global climate indices. If similar oscillatory patterns appear in the regional climatology of our study area that mimic global climate index oscillations, then a case could be made that a forcing pattern from the global climate index is also present in the regional climatology. The regional temperature anomaly's periodicity was proven to be on the same oscillation pattern of the AMO, as seen in Figure 17. The data supports the premise that the AMO plays a role, or is incorporated with, regional temperature decadal changes in the North Central Texas region. The precipitation anomaly data showed numerous oscillatory peaks on a shorter decadal trend ranging from 2 years - 13 years. While the precipitation power spectrum does show similarities with the ENSO oscillatory period, the overall spectrum power is too low, with a maximum value around 20 PSD, to prove conclusive on any single forcing oscillation, as observed in Figure 17. The overall low values in the power spectrum also exhibits the large amount of noise that is present in precipitation data.

In order to quantify whether changes in regional precipitation occurred during changes in climate index phases, precipitation distributions were plotted and compared. The precipitation probability density functions and cumulative distribution functions confirmed deviations of precipitation mean states when controlling for global climate indices phases. The AMO and ENSO events produced the largest discriminations in base states while the PDO exhibited little to no changes except for its seasonal relationship to ENSO events (Figures 19-21). Regional winter precipitation in North Central Texas is influenced by ENSO events (Figure 22), whereas spring precipitation is affected by a combination of both AMO and ENSO variability (Figures 24 and 25). In particular, AMO phases have the highest correlation to the changes in regional precipitation states, except for the case that a strong ENSO event occurs. In this case, the winter and spring time precipitation are determined by the type of ENSO event occurring. La Niña events generated a bimodal peak (Figures 19 and 25) in the precipitation probability density function, while El Niño events created a single peak. Thus, the North Central Texas regional precipitation is affected by La Niña events characterized by two separate non-Gaussian distributions, whereas El Niño events are typically normal Gaussian distributed. While there is a larger chance that below average winter precipitation are linked to La Niña events, there appears to be a similar chance that above-normal spring precipitation is controlled by either a La Niña or El Niño event. Thus, La Niña events influences the annual precipitation probability density with a bimodal peaking.

The statistical analyses suggest that a conditional streamflow ensemble be created in reference to AMO phase changes (e.g. streamflow and precipitation forecasts limited to similar AMO phase years) except in the case of El Niño or La Niña events, which will require a separate conditional streamflow ensemble created in reference to ENSO events. However, the separate conditional streamflow ensemble for ENSO events may prove

currently unfeasible as a streamflow ensemble requires a minimum of 20 years of data for accurate results, and the TRWD only has streamflow data from 1960-2016, which contain only 11 years of La Niña events and 17 years of El Niño events. The only option to circumvent this obstacle, without waiting for future data collection, would be to generate additional ensemble members within currently observed El Niño La Niña precipitation patterns, though applying that methodology would have the drawback of assuming future El Niño and La Niña events would fall within past parameters.

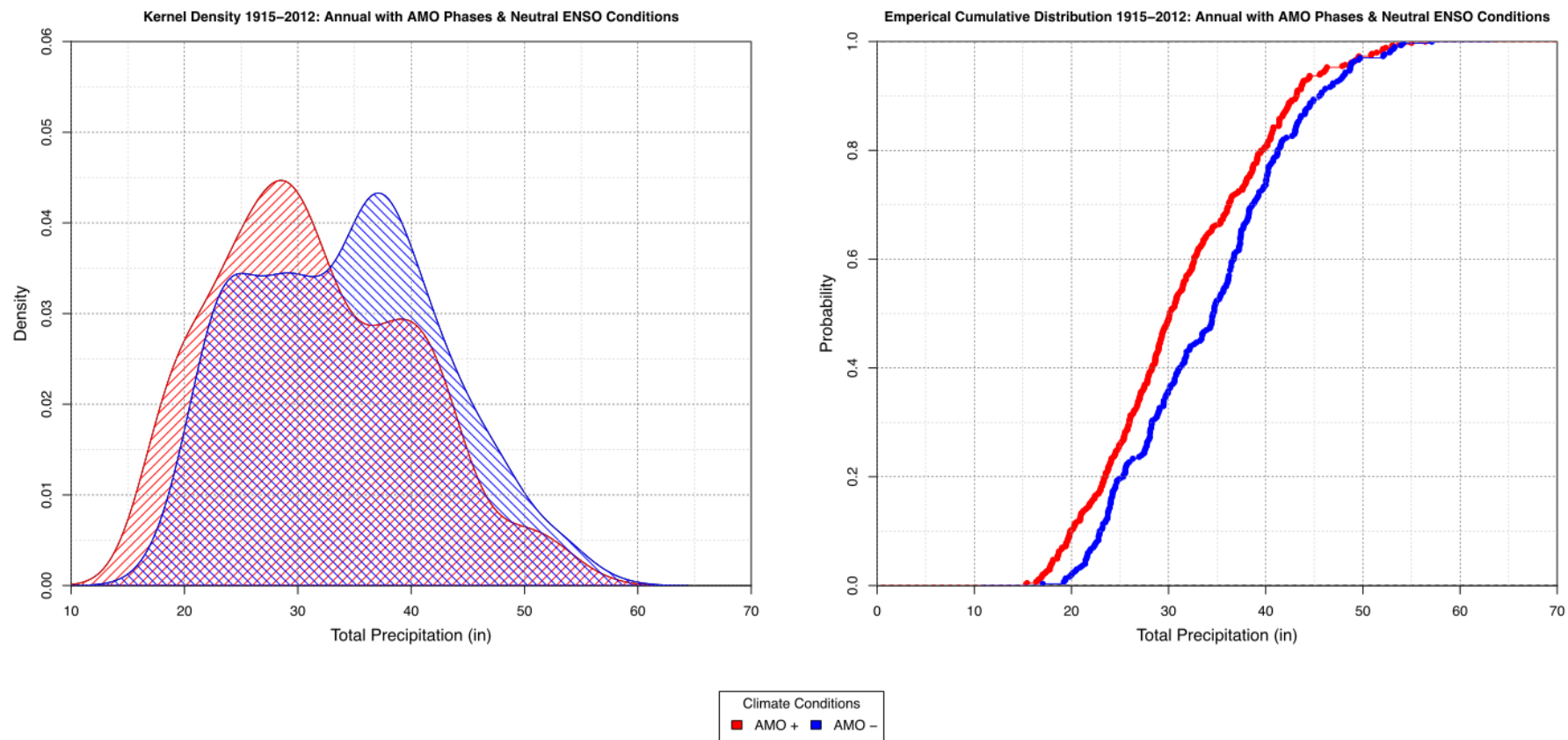


Figure 18: Probability density function (left) and cumulative distribution function (right) of total annual precipitation (in) from 1915-2012 for Trinity River Basin reservoirs during positive (red) and negative (blue) AMO phase years without La Niña and El Niño events. Note that 1 in = 25 mm.

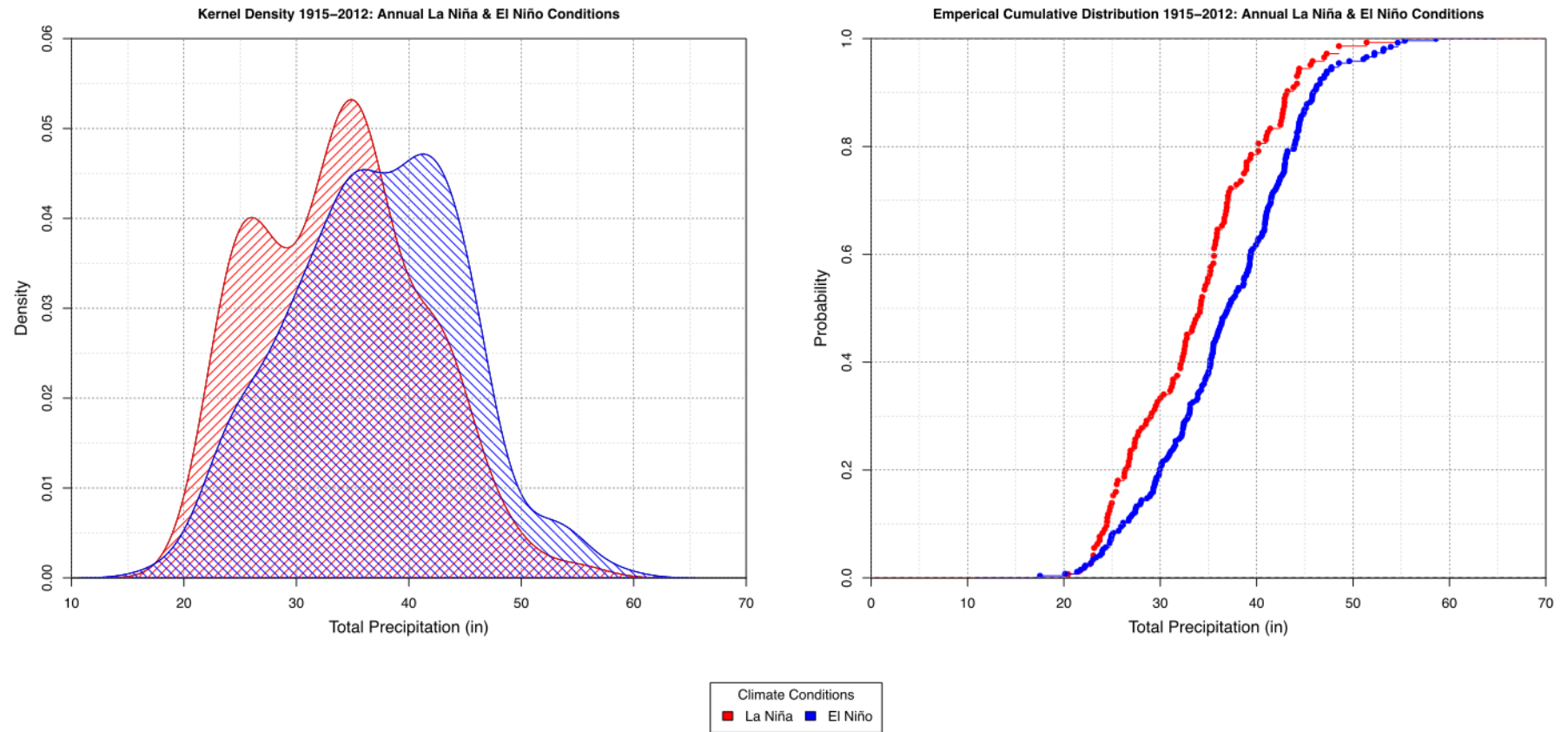


Figure 19: Probability density function (left) and cumulative distribution function (right) of total annual precipitation (in) from 1915-2012 for Trinity River Basin reservoirs during positive (red) and negative (blue) La Niña and El Niño event years. Note that 1 in = 25 mm.

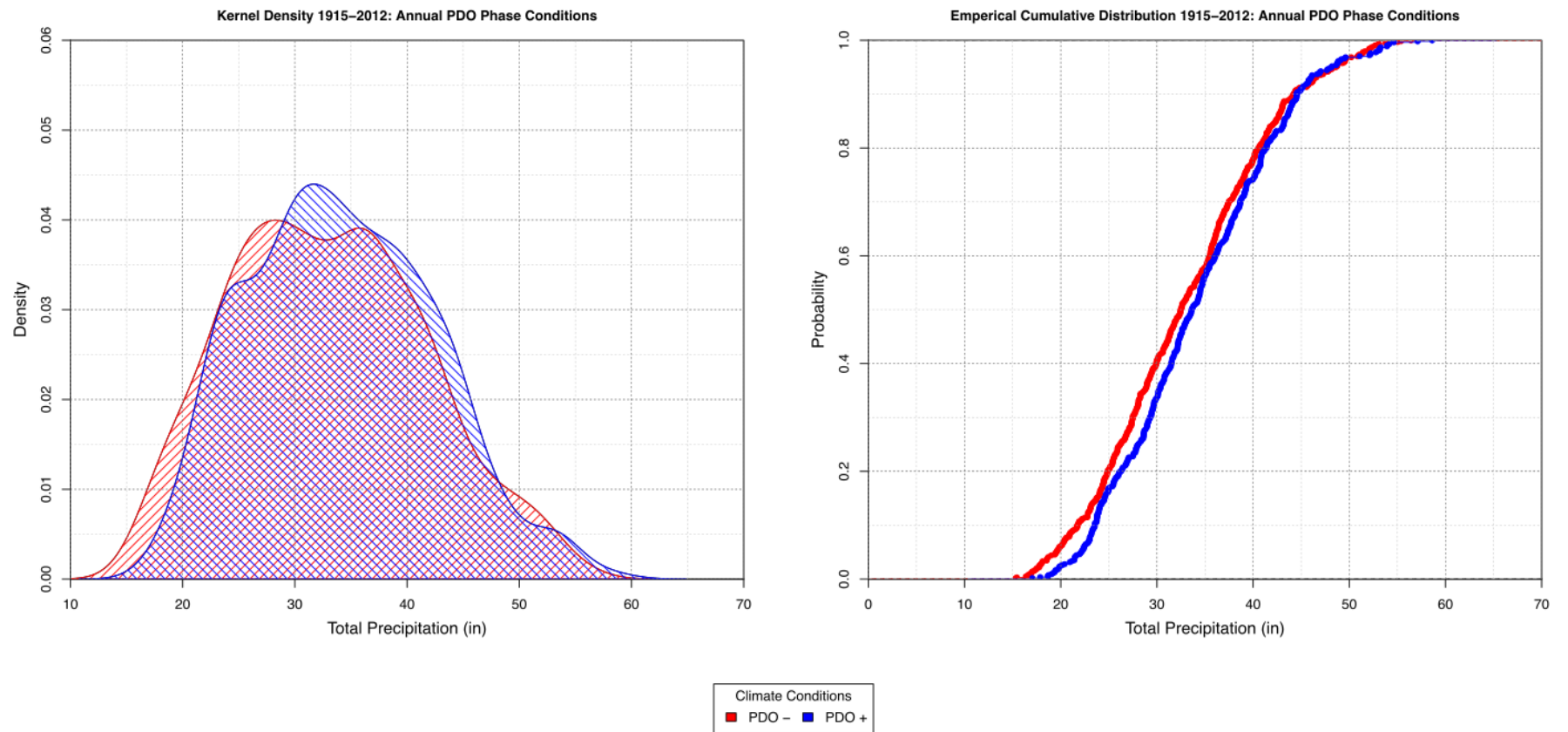


Figure 20: Probability density function (left) and cumulative distribution function (right) of total annual precipitation (in) from 1915-2012 for Trinity River Basin reservoirs during positive (blue) and negative (red) PDO phase years. Note that 1 in = 25 mm.

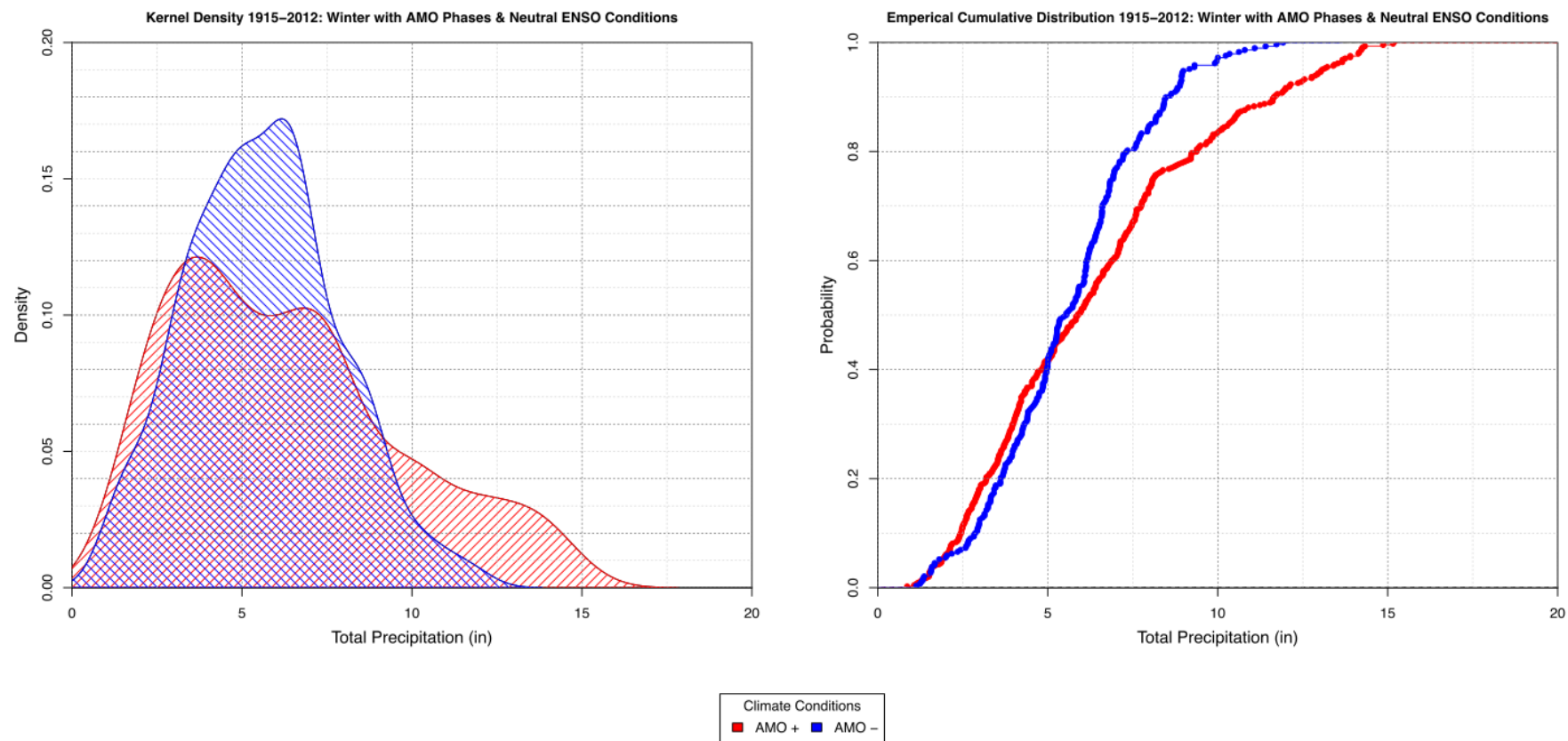


Figure 21: Probability density function (left) and cumulative distribution function (right) of total winter (Dec-Feb) precipitation (in) from 1915-2012 for Trinity River Basin reservoirs during positive (red) and negative (blue) AMO phase years without La Niña and El Niño events. Note that 1 in = 25 mm.

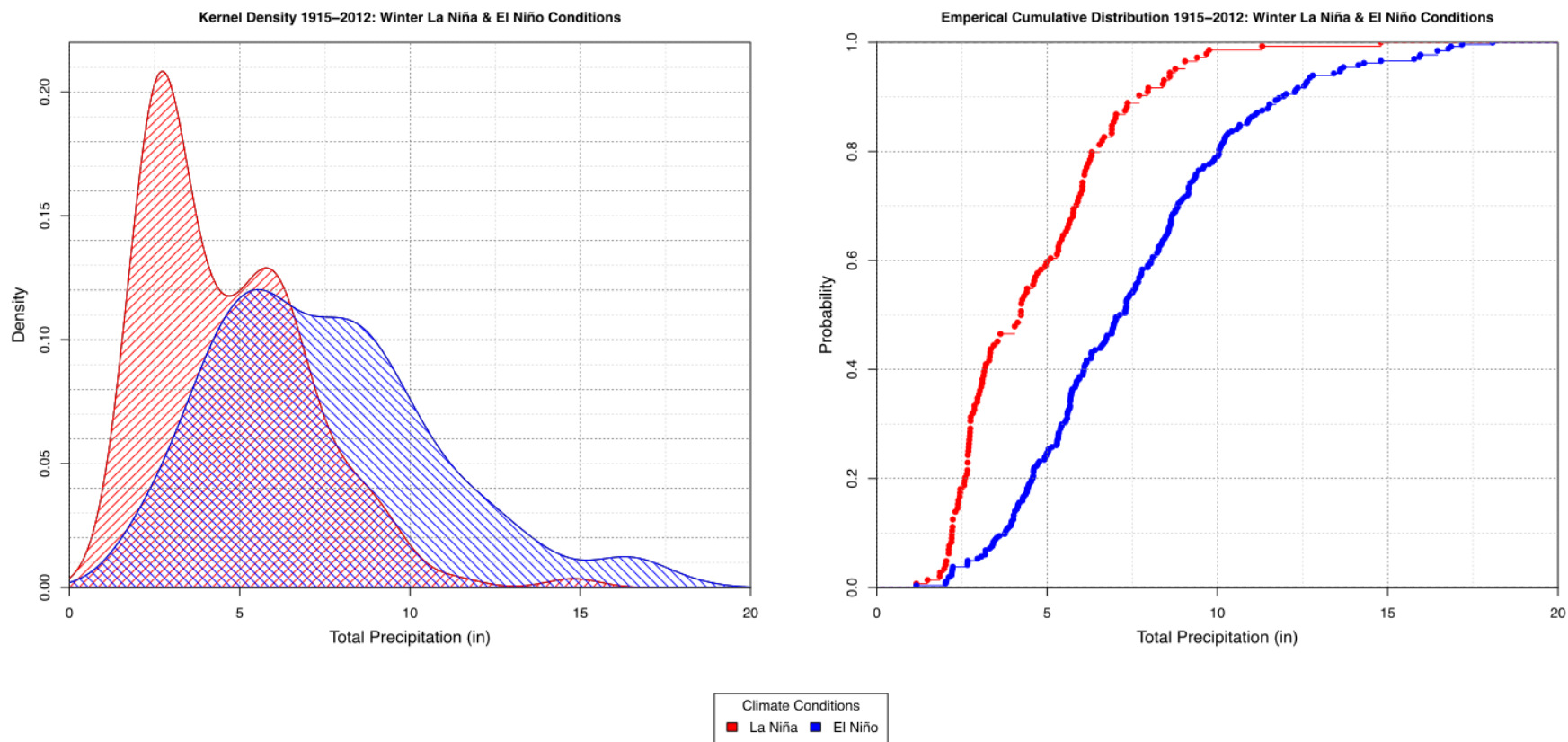


Figure 22: Probability density function (left) and cumulative distribution function (right) of total winter (Dec-Feb) precipitation (in) from 1915-2012 for Trinity River Basin reservoirs during positive (red) and negative (blue) La Niña and El Niño event years. Note that 1 in = 25 mm.

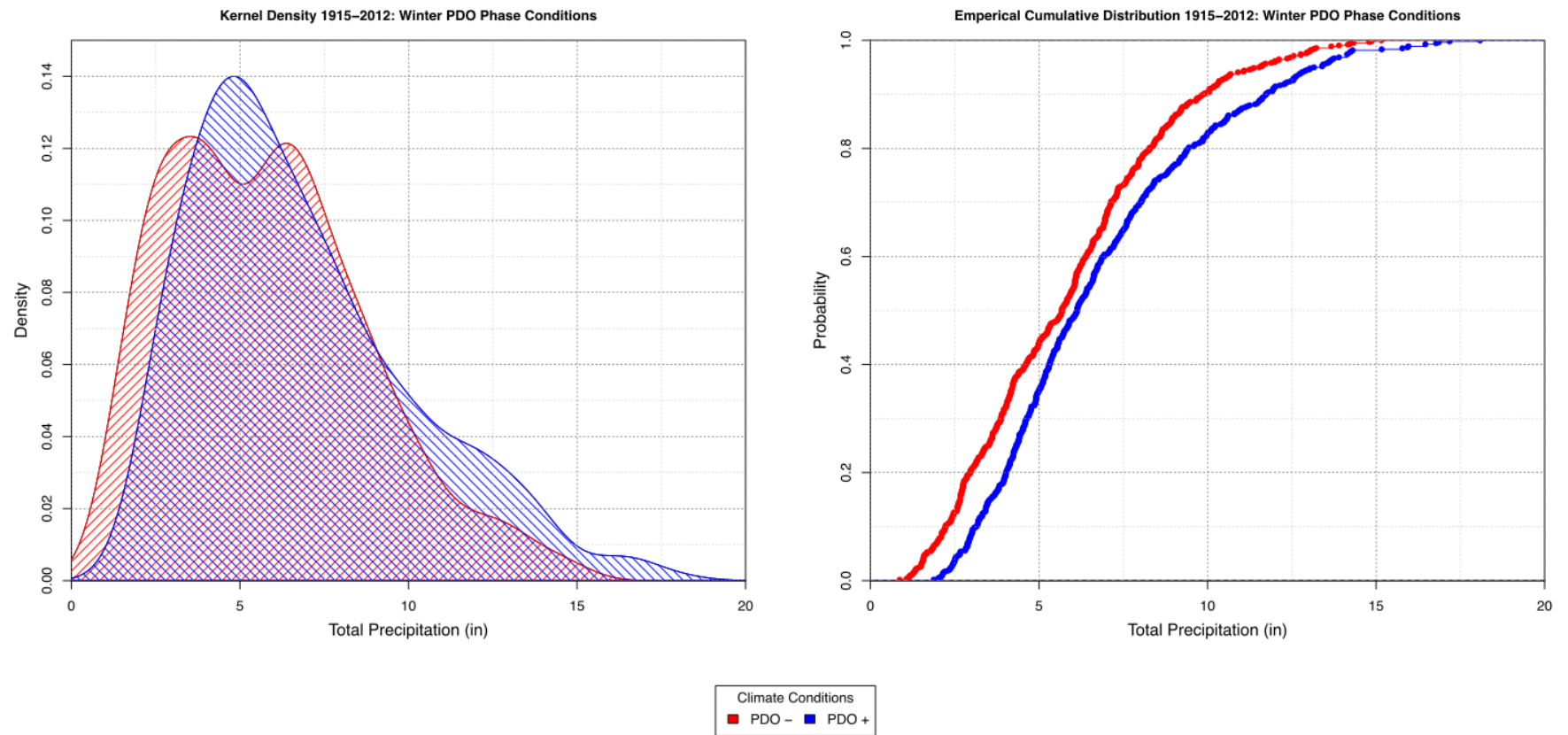


Figure 23: Probability density function (left) and cumulative distribution function (right) of total winter (Dec-Feb) precipitation (in) from 1915-2012 for Trinity River Basin reservoirs during positive (blue) and negative (red) PDO phase years. Note that 1 in = 25 mm.

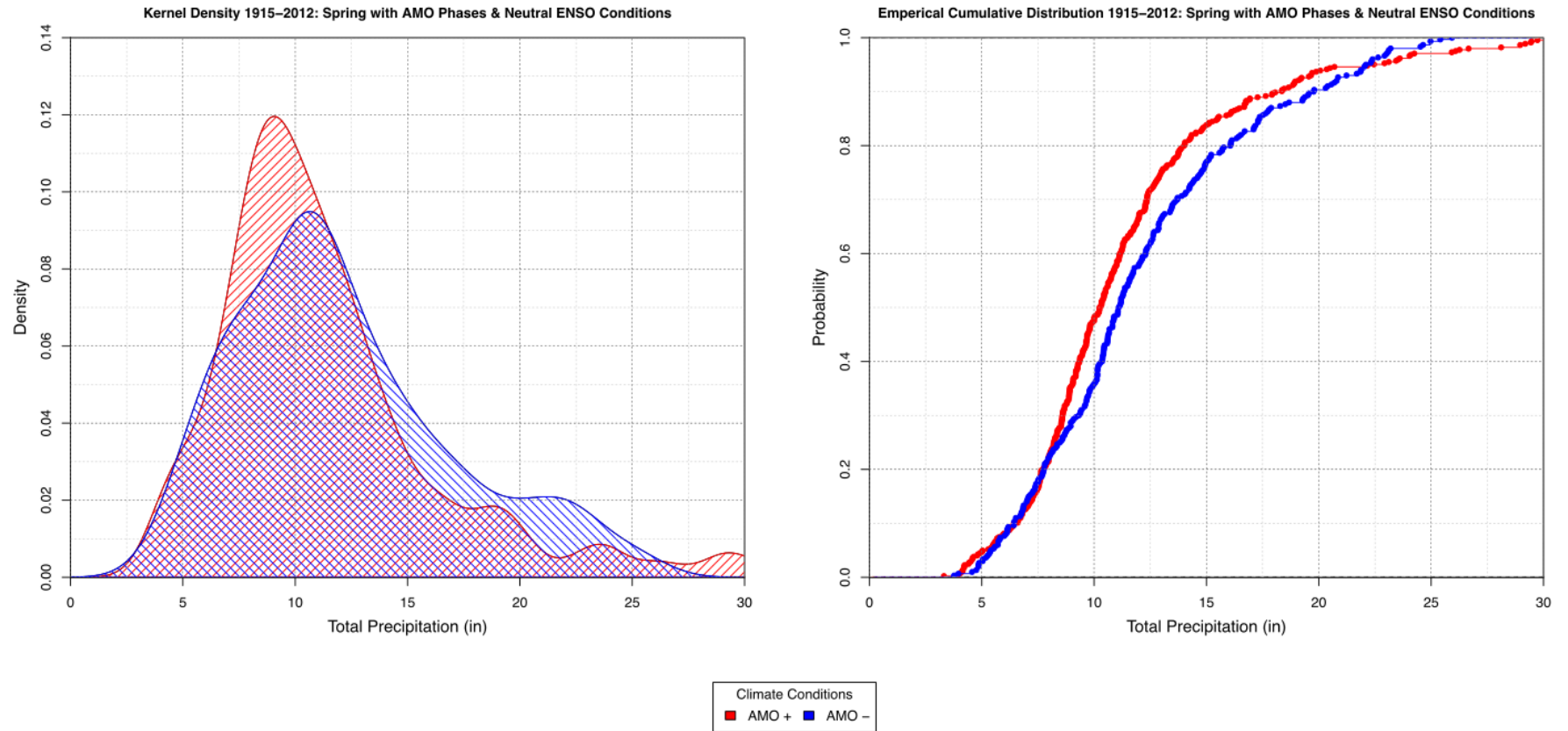


Figure 24: Probability density function (left) and cumulative distribution function (right) of total spring (Mar-May) precipitation (in) from 1915-2012 for Trinity River Basin reservoirs during positive (red) and negative (blue) AMO phase years without La Niña and El Niño events. Note that 1 in = 25 mm.

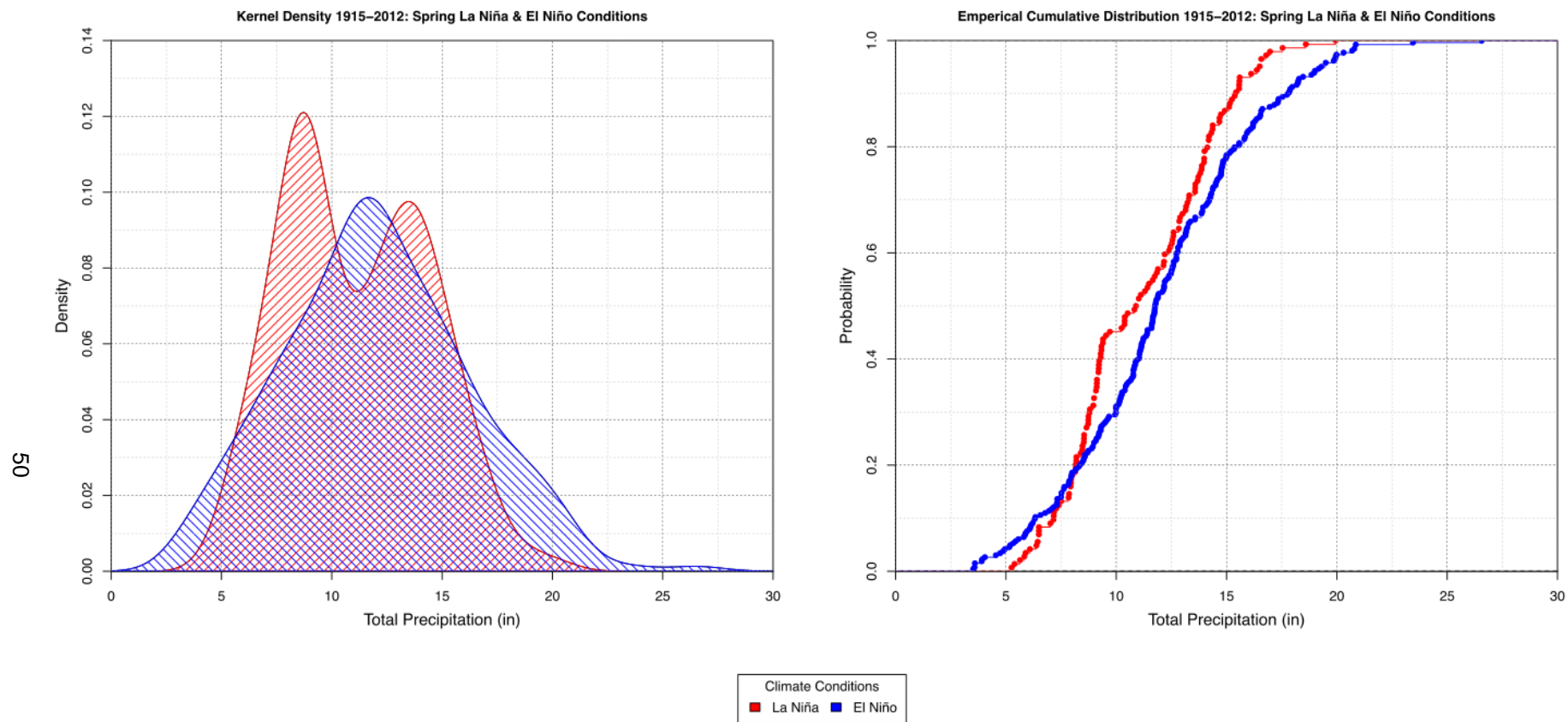


Figure 25: Probability density function (left) and cumulative distribution function (right) of total spring (Mar-May) precipitation (in) from 1915-2012 for Trinity River Basin reservoirs during positive (red) and negative (blue) La Niña and El Niño event years. Note that 1 in = 25 mm.

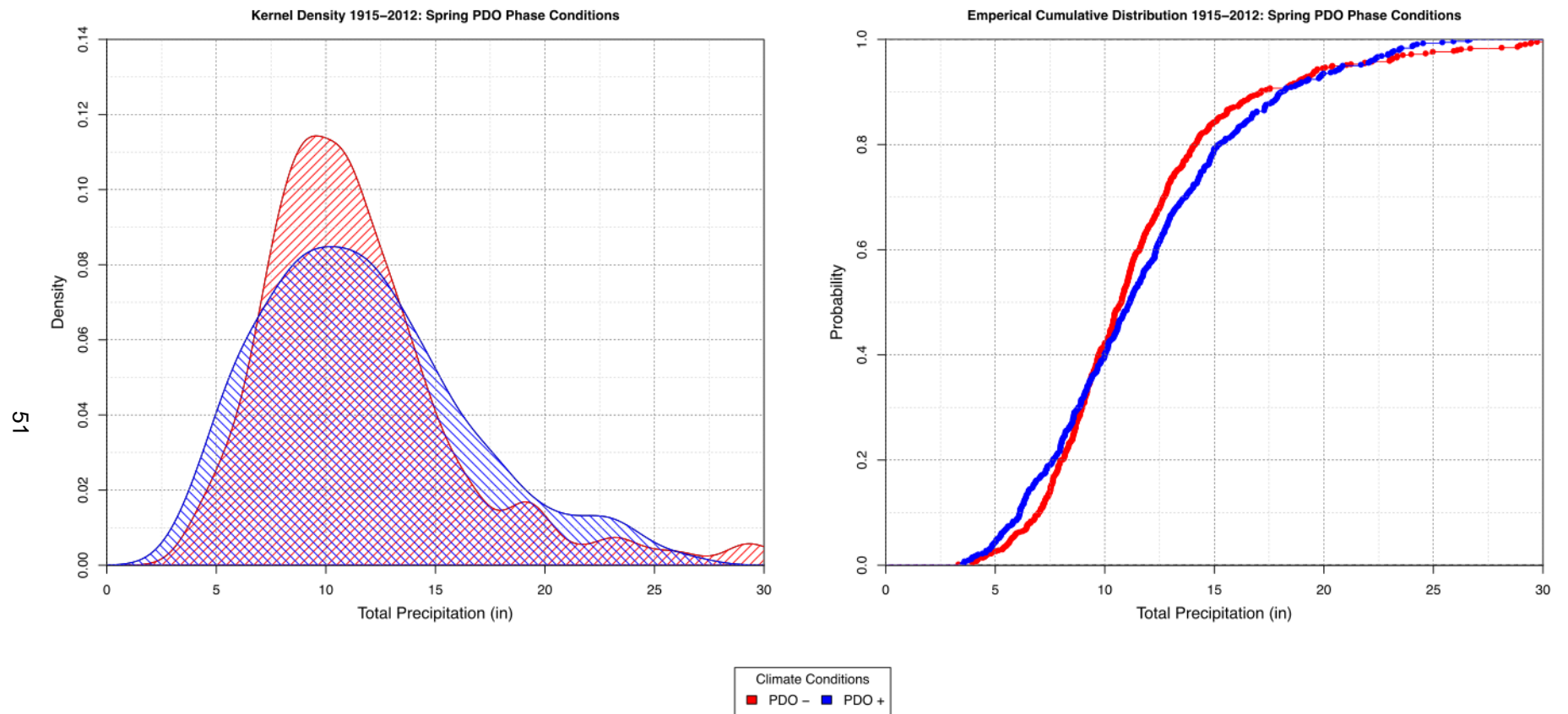


Figure 26 Probability density function (left) and cumulative distribution function (right) of total spring (Mar-May) precipitation (in) from 1915-2012 for Trinity River Basin reservoirs during positive (blue) and negative (red) PDO phase years. Note that 1 in = 25 mm.

Chapter 5

Hydrometeorological Forecasting

5.1 Artificial Neural Network (ANN) Model Results

The ANN model was run on a total of 9 out of the 18 reservoir catchment areas in the Tarrant Regional Water District, indicated in Figure 27 with a red triangle. The selected stations cover most parts of the Trinity River basin considered in this study. The averaged hydrometeorological data for these selected stations are comparable to the corresponding average of all stations and thus give an accurate estimation of the overall ANN model effectiveness. Note, that the ANN forecast skill is dependent on how well the chosen stations reflect the regional climate variability. The overall forecasting error and brier skill score (Eq. 16) was then calculated by averaging all of the reservoir catchment modeling results. These results were then related to other ANN model runs involving limited data inputs (e.g. removing climate indices, evaporation variables, temperature data, and precipitation data). From this, the amount of forecasting skill imparted by the data inputs on the ANN model by lead month was quantified (Figure 28), which shows the ANN model forecasting skill imparted by each data input on forecasting the SPEI 6-month drought index by lead time in months.

The incorporation of evaporation variables into the ANN model generated the greatest increase in forecasting skill starting at 58% at 1-month lead time. The model's skill utilizing the evaporation variables diminishes quickly with a skill of 0.0% at 4.5 months lead time. Until 5 months lead time, a positive forecast skill score around 20% is achieved for both precipitation and temperature values, with a slightly greater skill if only precipitation values. ANN models utilizing climate indices consistently produced a negative skill score throughout all forecasts and did not improve regional SPEI forecasting. Utilizing all positive

skill forecasting variables, an optimal ANN model forecasting skill score was achieved (Figure 28).

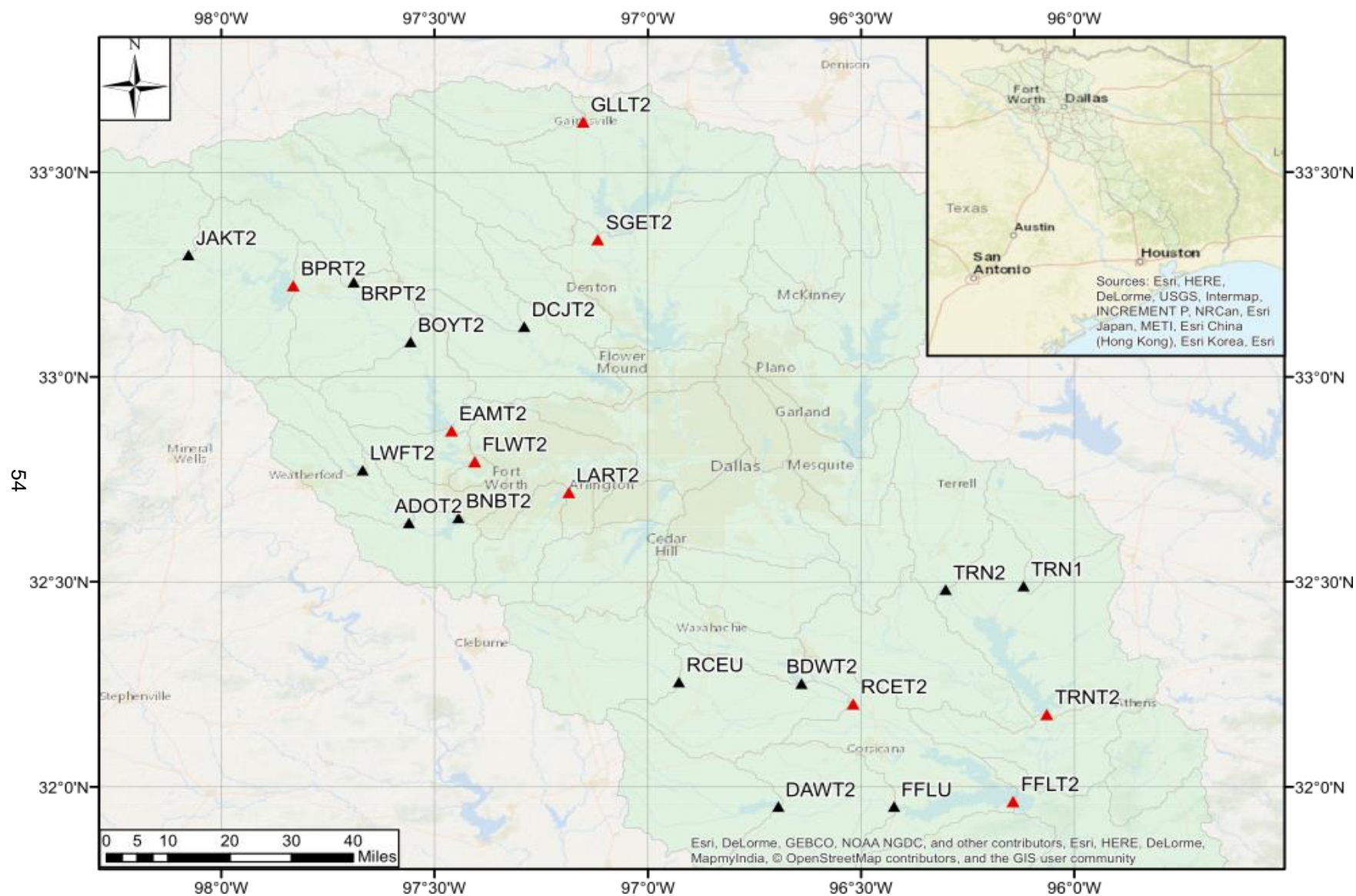


Figure 27: Tarrant Regional Water District reservoir catchment stations. Stations used in ANN modeling marked in red.

ANN SPEI Forecasting: Comparing Data Inputs

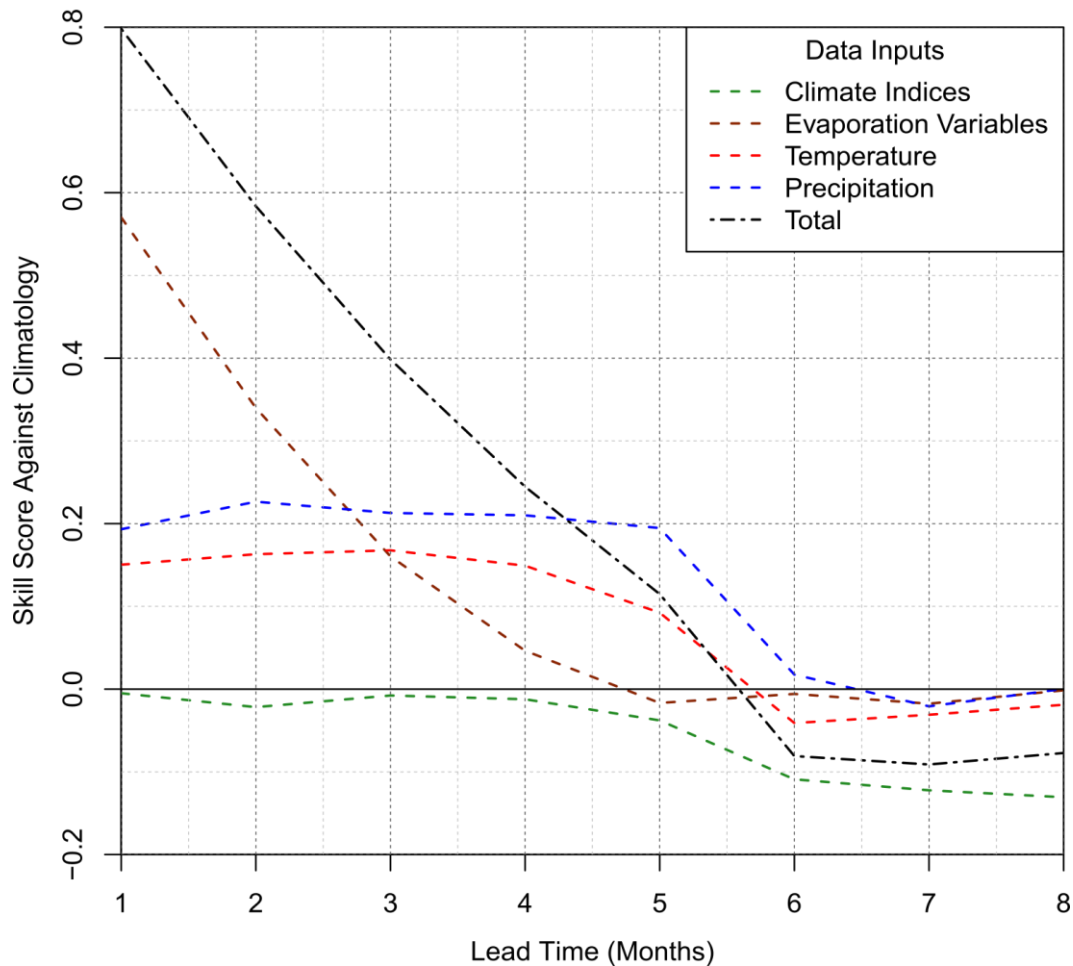


Figure 28: Brier's forecast skill score against climatology in regards to input variables such as temperature (red), precipitation (blue), and evaporation variables (brown). Also shown is the skill score using global climate indices only (green; AMO, PDO, ENSO) and total forecast using positive skill variables (black).

The total forecasting skill score (Figure 28) starts at 80% for a 1 month lead time before its decline below 20% after 4 months. To visualize the deteriorating forecast skill with lead time, model testing data for reservoir station SGET2 was plotted for 1-6 months lead time with the model forecasted SPEI (Figure 29-34). The ANN model begins with a

relatively high forecast skill because it starts with a fit to the observed data and slowly deteriorates over time to the SPEI's natural variability. There also appears to be a discrepancy in curve fitting and forecast skill when comparing SPEI values outside a -1 to 1 range, as seen in Figure 29. In order to quantify how much this might decrease predictive forecasting of droughts, the modeling error shown in Table 3 was generated while controlling for forecasting only moderate-extreme drought conditions. There was an overall increase in model mean absolute error and a decrease in the Pearson correlation (R^2) coefficient of determination when compared to the model predictions for all conditions resulting in a decreased forecasting lead time from 3-4 months for all conditions, to only 2-3 months for moderate – extreme drought forecasting. Thus, the ANN model has greater difficulty in the prediction of moderate-extreme drought conditions.

SPEI Forecast (months lead time)	All Conditions		Drought conditions	
	Mean Absolute Error (MAE)	R^2	Mean Absolute Error (MAE)	R^2
1	0.352	0.803	0.368	0.790
2	0.515	0.593	0.651	0.501
3	0.632	0.412	0.782	0.371
4	0.714	0.261	0.968	0.213
5	0.766	0.134	1.021	0.026
6	0.857	-0.057	1.323	0.006

Table 3: Model forecasting mean absolute error (MAE) and Pearson R^2 coefficient of determination for all SPEI conditions and moderate to extreme drought conditions (SPEI < -1.0).

5.2 Discussion

The ANN model was successful in forecasting drought conditions up to 2-3 months in advance of their occurrence through the use of the following regional climatology variables: minimum and maximum temperature, precipitation, and evaporation variables such as wind speed, evaporation, and potential evapotranspiration. The most important forecasting input for the model were the monthly potential evapotranspiration (PET) and wind speed. The importance of these variables are supported by other studies showing how regional PET fluctuations over time are easier to plot and predict than precipitation anomalies and how PET proves useful in forecasting drought indices [Trajkovic *et al.*, 2003]. The model forecasting skill of PET, however, decreased linearly with monthly lead time demonstrating that evaporation variables are temporally constrained and fluctuate the farther out from the month of collection [Torres *et al.*, 2011]. As such, while incorporating PET in ANN models may greatly increase the forecast skill at one-month lead time by 58%, it marginally rises the model forecasting capabilities by 2% at four-months lead time. In contrast to PET and wind speed, both temperature and precipitation variables give a near constant increase in model forecasting skill out to a five-month lead time. The ANN model utilizes the current monthly temperature and precipitation values in order to determine the most likely temperature or precipitation regime and generate a constant improvement of SPEI forecasting. For example, if precipitation monthly values are lower than average, the model will increase forecasting skill by weighting forecasted drought index values to drought conditions. In contrast to generating a large skill increase, it would generate a consistent skill increase that would approach zero at the end of the time step for the drought index, due to the fact that the previous drought condition leads to a retention of the state.

When the global climate indices were incorporated into the ANN model, forecasting skill decreased across all stations and climate indices creating an inconsistency with the previous chapter's research, as it was shown that both the AMO and ENSO events contribute to an overall deviation in the precipitation probability distribution mean state. Raising the question of why the model did not improve with this proven teleconnection into the drought forecasting. Due to the black box nature of ANN models, the only statistical information the ANN model can give us is the fact that global climate indices did not improve regional drought predictions, leaving the reasoning as to why this occurred open to interpretation. It is our conjecture that the ANN model did not incorporate the multi-decadal climate indices as the shifts in precipitation probability density would be unnecessary with precipitation values as model inputs. The model would use a current month's precipitation data to determine the precipitation regime, which is unlikely to change in a 5-month time step from decadal variability. Therefore, multi-decadal global climate indices with influences on precipitation patterns would be redundant in this context. In the case of shorter term ENSO events, the lack of forecasting skill could be derived from the forecasting model being trained on a long time series and fitted to normal climatological conditions. The infrequency of ENSO events would lower the average drought model forecasting skill and result in a decrease in average model performance, as the ENSO index becomes only significant during ENSO events. There is also the possibility that the spatial distance of the North Central Texas region from these global climate indices reduced the variables' ability to improve forecasting skill. ANN drought modeling of coastal Australia and the Pacific Northwest often incorporates the use of the Nino 3.4 index, as climate conditions in these regions are affected to a greater extent by the Pacific's climate conditions [Deo and Şahin, 2015; Silverman and Dracup, 2000]. These studies did not include data on varying their ANN model inputs, so it is impossible to determine the overall

model forecasting skill improvements from the incorporation of the Nino 3.4 index in related studies.

Finally, this ANN modeling scheme was able to accurately predict 2-3 months in advance by incorporated only the SPEI with a 6-month time step. These findings are reflected in other ANN modeling studies which generated predictions of 2-3 months in advance, though those studies used the SPEI with an annual time step. If this study's ANN model was retrained on the SPEI with an annual time step, an increase in forecasting lead time would be expected due to the nature of drought indices serial correlation to previous values.

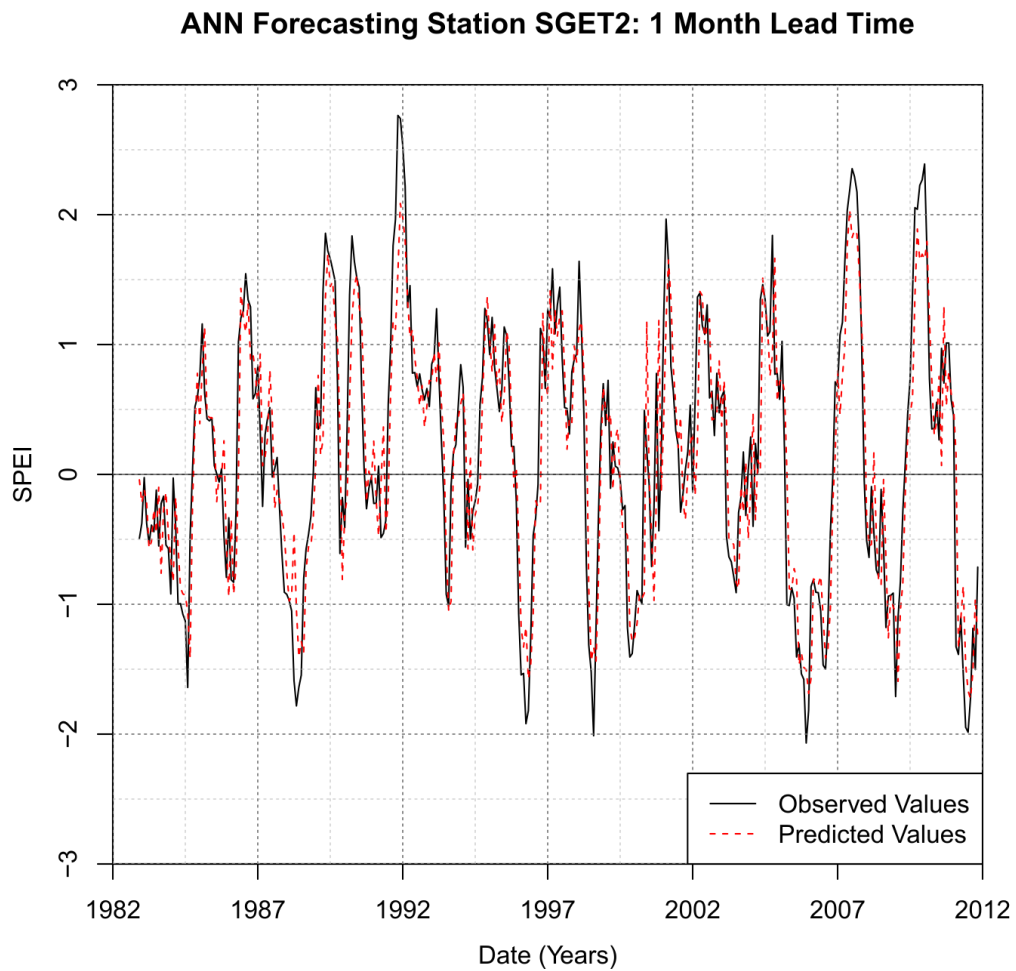


Figure 29: SPEI 6 month drought index values for reservoir catchment SGET2 from 1983-2012 with black representing actual values and red the ANN model 1 month in advance predicted values.

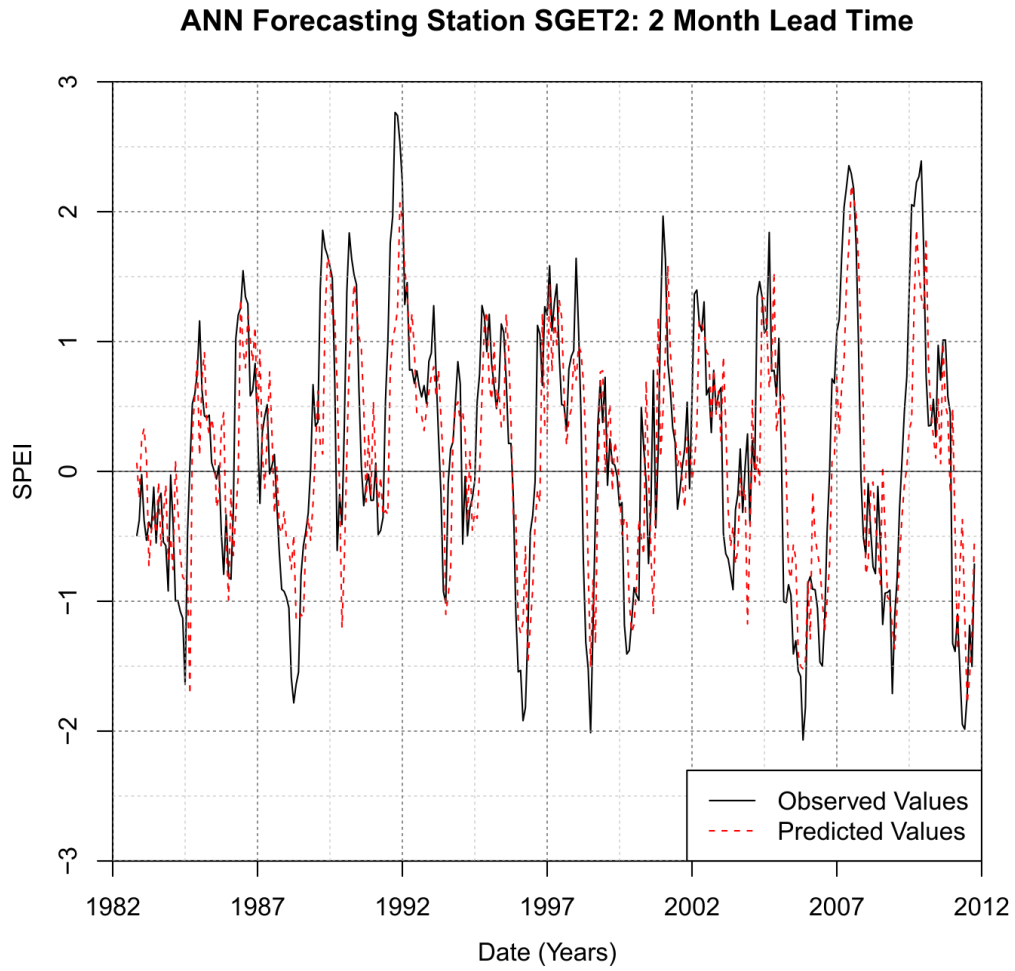


Figure 30: SPEI 6 month drought index values for reservoir catchment SGET2 from 1983-2012 with black representing actual values and red the ANN model 2 month in advance predicted values.

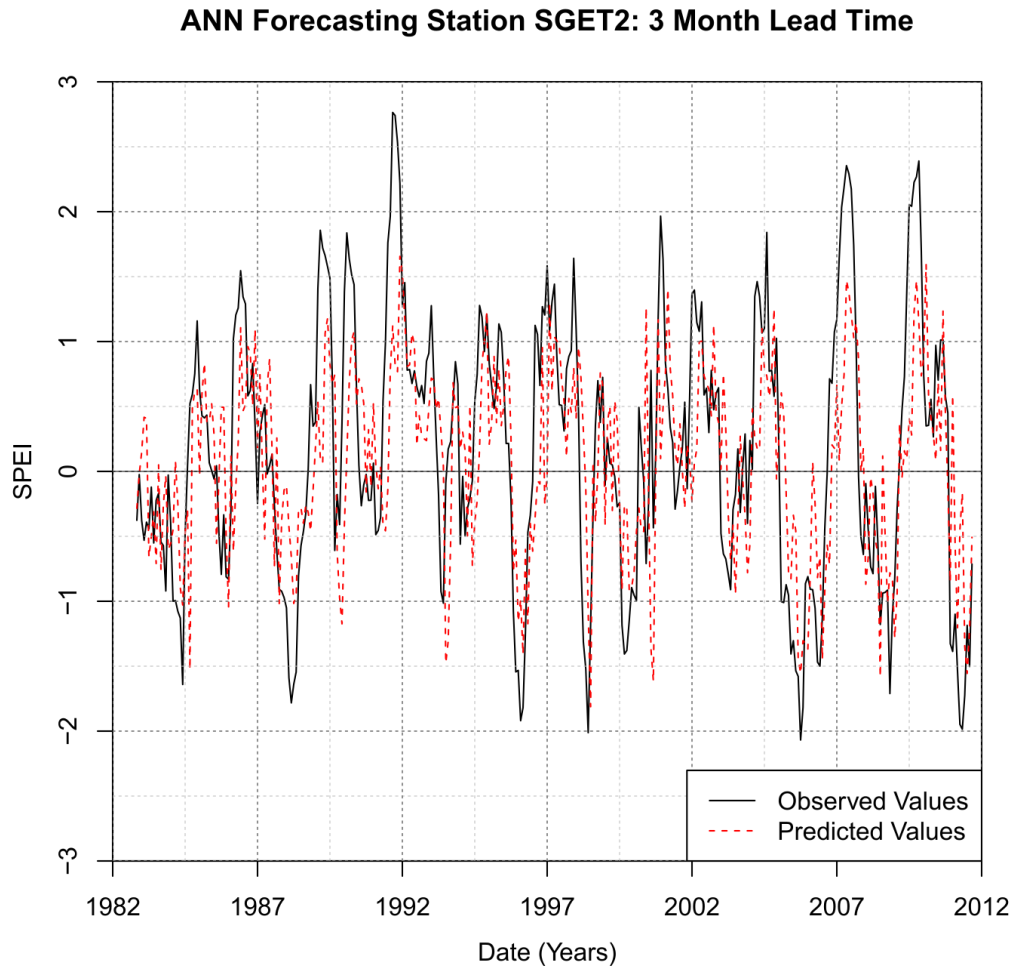


Figure 31: SPEI 6 month drought index values for reservoir catchment SGET2 from 1983-2012 with black representing actual values and red the ANN model 3 month in advance predicted values.

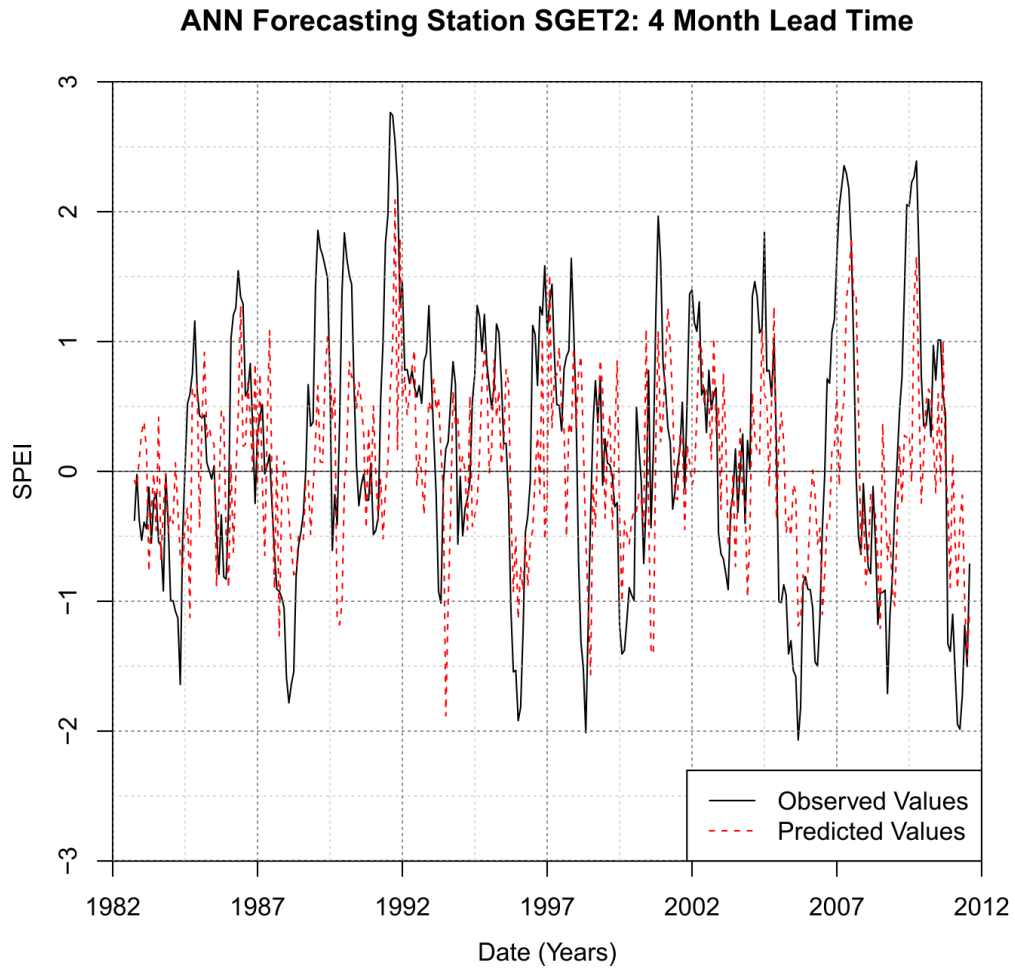


Figure 32: SPEI 6 month drought index values for reservoir catchment SGET2 from 1983-2012 with black representing actual values and red the ANN model 4 month in advance predicted values.

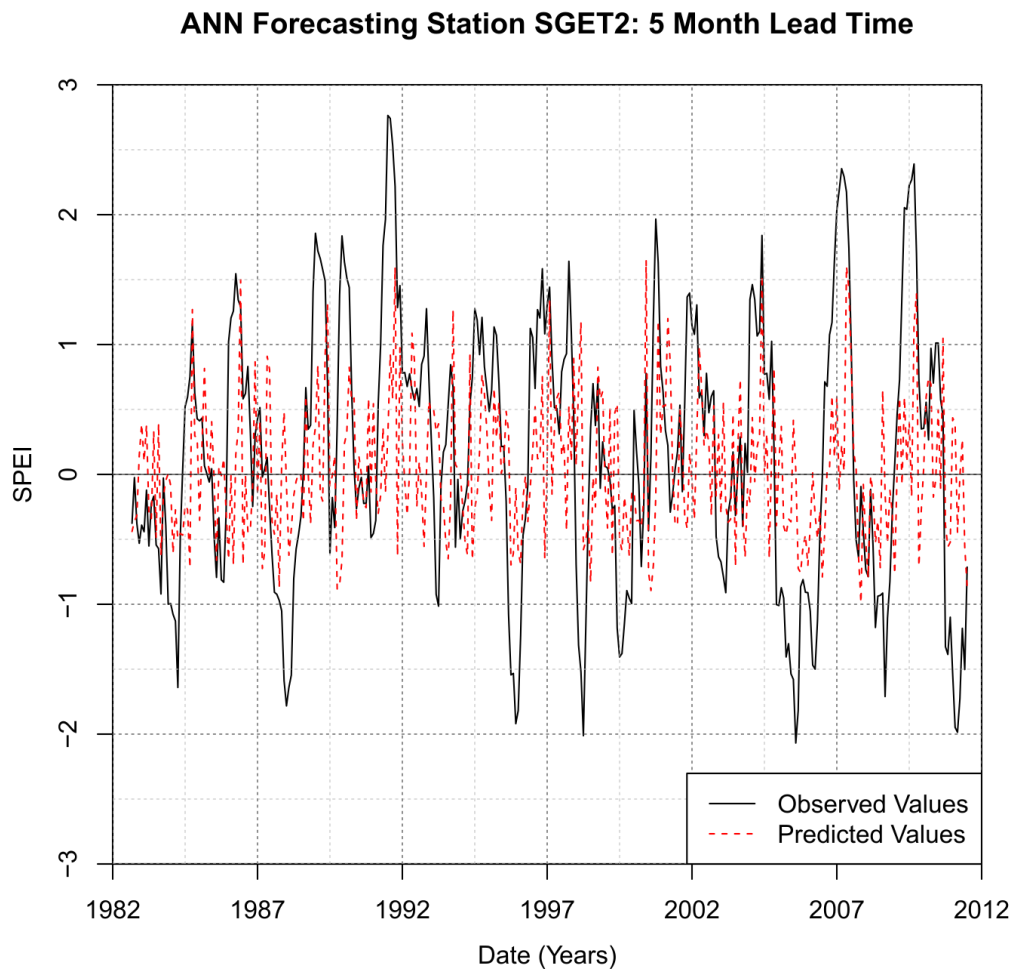


Figure 33: SPEI 6 month drought index values for reservoir catchment SGET2 from 1983-2012 with black representing actual values and red the ANN model 5 month in advance predicted values.

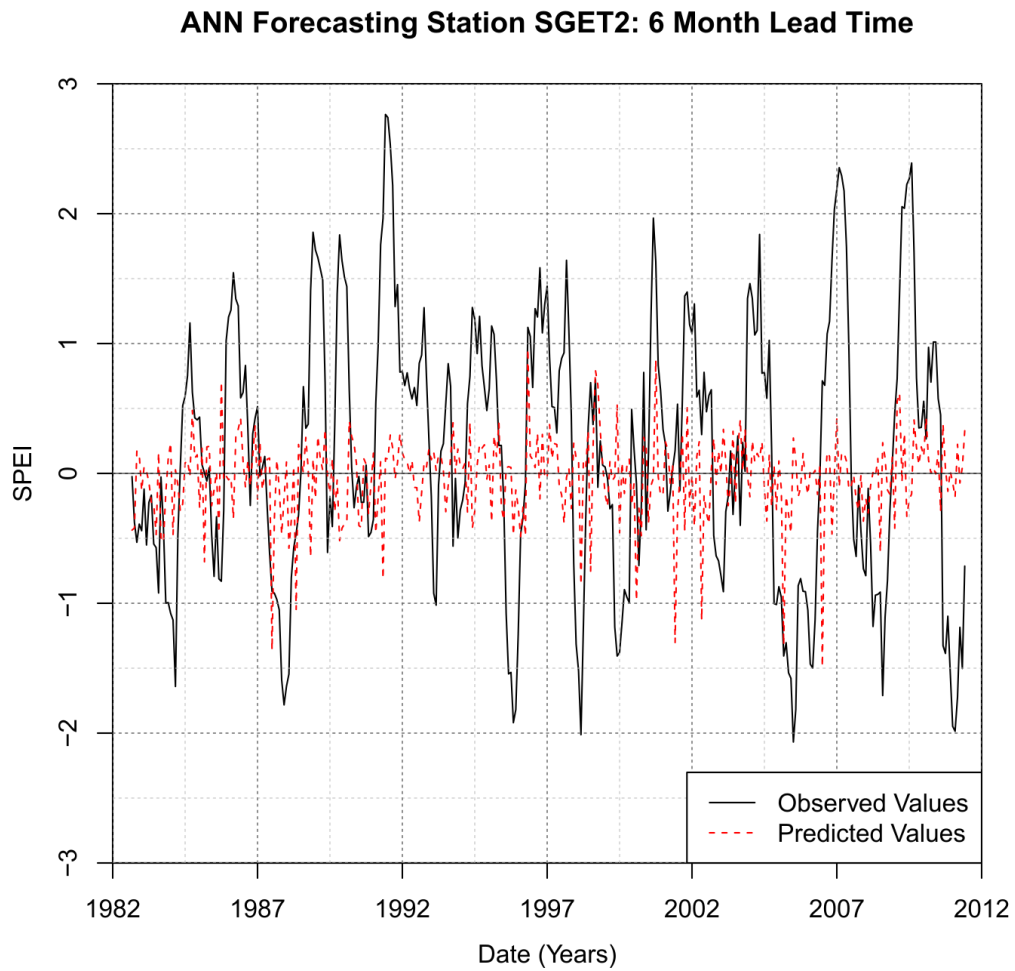


Figure 34: SPEI 6 month drought index values for reservoir catchment SGET2 from 1983-2012 with black representing actual values and red the ANN model 6 month in advance predicted values.

Chapter 6

Conclusion

The Tarrant Regional Water District is increasingly vulnerable to weather anomaly events, such as prolonged droughts and flash floods, with an increasing population and growing water demand. In order to prevent and limit the amount of damage that these weather anomaly events can cause, this study evaluates and increases the forecasting ability of the Hydraulic Ensemble Forecasting System and predict reservoir hydrometeorological conditions with Artificial Neural Network modeling. Analysis of teleconnections of global climate indices with North Central Texas precipitation distributions suggested that an implementation of a conditional ensemble streamflow prediction, with focus on AMO phases and ENSO events, into HEFS should generate an increase in forecasting skill. As of this publication, the implementation of the conditional ensemble streamflow prediction into HEFS is still undergoing statistical testing in the Tarrant Regional Water District. Further research is needed to explore how the AMO climate phases and ENSO events interact with each other under global climate change and affect the North Central Texas region. Also, further investigations are required to evaluate the cause of the bimodal La Niña precipitation probability density function. This could result in a better understanding of dominant processes that may contribute to regional drought conditions.

The study presented here demonstrated that the use Artificial Neural Network (ANN) modeling should be incorporated into reservoir management as an additional tool to estimate future reservoir hydrometeorological conditions up to 2-3 months ahead. Through the collection of mean areal precipitation, mean areal temperature, wind speed, and potential evapotranspiration, ANN modeling requires further development in regards

to being trained on the SPEI 3 month and 12 month time steps and the addition of spatial variability inputs. Adding spatial variability would allow multiple reservoir forecast off one model and with the inclusion of the SPEI 3 and 12-month time steps drought indices could be forecasted on the seasonal, semi-annual, and annual level. Hybrid ANN models, which incorporate fuzzy logic components or wavelet signal deconstruction analysis, also require further research as they have shown promise in generating better drought forecasting results than models with only an ANN structure [Özger *et al.*, 2012]. Presently, hybrid ANN models have only been used in statewide drought forecasting and require testing on a regional basis. An implementation of this model into a drought forecast would require a consistent sampling of regional hydrological data at reservoir stations (such as in the TRWD district) and archiving of the data into a database. Temperature data collection is particularly important as it is primarily utilized in the derivation of potential evapotranspiration, a key component of meteorological droughts as shown in this research. In contrast, only mean areal precipitation data is currently collected for the TRWD reservoir catchment areas.

The regional water management agencies, such as the Tarrant Regional Water District, would be better prepared to assess future water resources in response to severe weather and climate events by incorporating the above listed improvements and recommendations in existing hydraulic and drought forecasting tools. Continued research in improvements to current forecasting systems, by using high-resolution state of the art weather and climate models as well as hybrid ANN models is required to improve long-term forecast of droughts and flooding.

References

- Baawain, M. S., M. H. Nour, A. G. El-Din, and M. G. El-Din (2005), El Niño Southern-Oscillation prediction using Southern Oscillation Index and Niño3 as onset indicators: Application of artificial neural networks, *Journal of Environmental Engineering and Science*, 4(2), 113-121.
- Basheer, I., and M. Hajmeer (2000), Artificial neural networks: Fundamentals, computing, design, and application, *Journal of Microbiological Methods*, 43(1), 3-31.
- Beguiría, S., S. M. Vicente-Serrano, F. Reig, and B. Latorre (2014), Standardized precipitation evapotranspiration index (SPEI) revisited: Parameter fitting, evapotranspiration models, tools, datasets and drought monitoring, *International Journal of Climatology*, 34(10), 3001-3023.
- Bjerknes, J. (1964), Atlantic air-sea interaction, *Advances in Geophysics*, edited by H. E. Landsberg and J. V. Miegheem, Elsevier, 82 pp.
- Bjerknes, J. (1969), Atmospheric teleconnections from the Equatorial Pacific, *Monthly Weather Review*, 97(3), 163-172.
- Blackman, R. B., and J. W. Tukey (1958), The measurement of power spectra from the point of view of communications engineering — part i, *Bell System Technical Journal*, 37(1), 185-282, doi: 10.1002/j.1538-7305.1958.tb03874.x.
- Blaylock, L., T. Adams, and N. Mander (2016), Climate-based operational forecasting with examples from the Tarrant Regional Water District, accessed (February 13, 2017), adapted from <<http://riverware.org/riverware/ugm/2016/abstracts/AdamsEtAl.html>>.
- Booth, E., J. Mount, and J. H. Viers (2006), Hydrologic variability of the cosumnes river floodplain, *San Francisco Estuary and Watershed Science*, 4(2).

- Dai, A., I. Y. Fung, and A. D. Del Genio (1997), Surface observed global land precipitation variations during 1900–88, *Journal of Climate*, 10(11), 2943-2962, doi: 10.1175/1520-0442(1997)010<2943:SOGLPV>2.0.CO;2.
- Delworth, L. T., and E. M. Mann (2000), Observed and simulated multidecadal variability in the Northern Hemisphere, *Climate Dynamics*, 16(9), 661-676, doi: 10.1007/s003820000075.
- Demargne J., D.-J. Seo, L. Wu, and J. Schaake (2007), Experimental hydrometeorological and hydrological ensemble forecasts and their verification in the U.S. National Weather Service, IAHS-AISH publication, pp. 177-187.
- Demargne, J., L. Wu, S. K. Regonda, H. Lee, M. He, D.-J. Seo, R. Hartman, H. D. Herr, M. Fresch, J. Schaake, and Y. Zhu. (2014), The science of NOAA's operational hydrologic ensemble forecast service, *Bulletin of the American Meteorological Society*, 95(1), 79-98, doi: 10.1175/BAMS-D-12-00081.1.
- Deo, R. C. and M. Sahin (2015), Application of the artificial neural network model for prediction of monthly standardized precipitation and evapotranspiration index using hydrometeorological parameters and climate indices in Eastern Australia, *Atmospheric Research*, 161, 65-81, doi: 10.1016/j.atmosres.2015.03.018.
- Donges, J. F., Y. Zou, N. Marwan, and J. Kurths (2009), Complex networks in climate dynamics, *The European Physical Journal Special Topics*, 174(1), 157-179.
- Droogers, P., and R. G. Allen (2002), Estimating reference evapotranspiration under inaccurate data conditions, *Irrigation and Drainage Systems*, 16(1), 33-45.
- Enfield, D. (2001), The Atlantic Multidecadal Oscillation and its relation to rainfall and river flows in the Continental U.S., *Geophysical Research Letters*, 28(10), 2077-2080.
- Fannin, B. (2012), Updated 2011 Texas agricultural drought losses total \$7.62 billion, *AgriLife TODAY*. accessed (December 7, 2017), adapted from

<<https://today.agrilife.org/2012/03/21/updated-2011-texas-agricultural-drought-losses-total-7-62-billion/>>

Flood, I., and N. Kartam (1994), Neural networks in civil engineering. li: Systems and application, Journal of Computing in Civil Engineering, 8(2), 149-162.

Furber, S., and S. Temple (2007), Neural systems engineering, Journal of The Royal Society Interface, 4(13), 193-206, doi: 10.1098/rsif.2006.0177.

Gilbeaux, K. (2013), Texas climate divisions, accessed (January 16, 2017), adapted from <<http://texas.resiliencesystem.org/texas-climate-divisions>>.

Gupta, H. V., K. J. Beven, and T. Wagener (2006), Model calibration and uncertainty estimation, Encyclopedia of Hydrological Sciences, John Wiley & Sons, Ltd., 131 pp..

Hamill, T. M., and J. Juras (2006), Measuring forecast skill: Is it real skill or is it the varying climatology?, Quarterly Journal of the Royal Meteorological Society, 132(621), 2905-2924.

Hamlet, A. F., and D. P. Lettenmaier (2000), Long-range climate forecasting and its use for water management in the Pacific Northwest region of North America, Journal of Hydroinformatics, 2(3), 163-182.

Hlinka, J., D. Hartman, M. Vejmelka, D. Novotná, and M. Paluš (2014), Non-linear dependence and teleconnections in climate data: Sources, relevance, nonstationarity, Climate Dynamics, 42(7-8), 1873-1886.

Hoerling, M., A. Kumar, R. Dole, J. W. Nielsen-Gammon, J. Eischeid, J. Perlwitz, X.-W. Quan, T. Zhang, P. Pegion, and M. Chen (2013), Anatomy of an extreme event, Journal of Climate, 26(9), 2811-2832, doi: 10.1175/jcli-d-12-00270.1.

Hornik, K., M. Stinchcombe, and H. White (1989), Multilayer feedforward networks are universal approximators, Neural Networks, 2(5), 359-366.

- Hu, Q., S. Feng, and R. J. Oglesby (2011), Variations in North American summer precipitation driven by the Atlantic Multidecadal Oscillation, *Journal of Climate*, 24(21), 5555-5570, doi: 10.1175/2011JCLI4060.1.
- Hurrell, J., and H. van Loon (1997), Decadal variations in climate associated with the North Atlantic Oscillation, *Climatic Change at High Elevation Sites*, Springer Netherlands, pp. 69-94.
- Hurrell, J. W. (1995), Decadal trends in the North Atlantic Oscillation: Regional temperatures and precipitation, *Science*, 269(5224), 676-679, doi: 10.1126/science.269.5224.676.
- Jacox, M. G., E. L. Hazen, K. D. Zaba, D. L. Rudnick, C. A. Edwards, A. M. Moore, and S. J. Bograd (2016), Impacts of the 2015–2016 El Niño on the California current system: Early assessment and comparison to past events, *Geophysical Research Letters*, 43(13), 7072-7080.
- Kahya, E., and J. A. Dracup (1994), The influences of type 1 El Niño and La Niña events on streamflows in the Pacific Southwest of the United States, *Journal of Climate*, 7(6), 965-976, doi: doi:10.1175/1520-0442(1994)007<0965:TIOTEN>2.0.CO;2.
- Karl, T. R., and R. G. Quayle (1981), The 1980 summer heat wave and drought in historical perspective, *Monthly Weather Review*, 109(10), 2055-2073, doi: doi:10.1175/1520-0493(1981)109<2055:TSHWAD>2.0.CO;2.
- Lapp, S. L., J.-M. St. Jacques, D. J. Sauchyn, and J. R. Vanstone (2013), Forcing of hydroclimatic variability in the Northwestern Great Plains since ad 1406, *Quaternary International*, 310, 47-61, doi: 10.1016/j.quaint.2012.09.011.
- Livneh, B., E. A. Rosenberg, C. Lin, B. Nijssen, V. Mishra, K. M. Andreadis, E. P. Maurer, and D. P. Lettenmaier (2013), A long-term hydrologically based dataset of land surface fluxes and states for the Conterminous United States: Update and extensions, *Journal of Climate*, 26(23), 9384-9392.

- Mantua, N. J., S. R. Hare, Y. Zhang, J. M. Wallace, and R. C. Francis (1997), A Pacific interdecadal climate oscillation with impacts on salmon production, *Bulletin of the American Meteorological Society*, 78(6), 1069-1079, doi: doi:10.1175/1520-0477(1997)078<1069:APICOW>2.0.CO;2.
- Minobe, S. (1997), A 50–70 year climatic oscillation over the North Pacific and North America, *Geophysical Research Letters*, 24(6), 683-686, doi: 10.1029/97GL00504.
- Montanari, A., and G. Grossi (2008), Estimating the uncertainty of hydrological forecasts: A statistical approach, *Water Resources Research*, 44(12), doi: 10.1029/2008WR006897.
- Newby, S., and J. M. Oliver (2016), Comprehensive annual financial report, *Rep.*, Tarrent Regional Water District. Arlington, 133 pp.
- Nicholls, N. (2001), Commentary and analysis: The insignificance of significance testing, *Bulletin of the American Meteorological Society*, 82(5), 981-986.
- NOAA (2016), El Niño & La Niña information, accessed (January 16, 2017), adapted from <<https://www.climate.gov/sites/default/files/LosNinoshighpressureHR.jpg>>.
- NOAA (2017), Equatorial Pacific sea surface temperatures, accessed (January 16, 2017), adapted from <<https://www.ncdc.noaa.gov/teleconnections/enso/indicators/sst.php>>.
- NWS (2015), DFW long term climate data, accessed (October 25, 2015), adapted from <<http://www.srh.noaa.gov/fwd/?n=dfwclimo>>.
- Ortengren, J. T., P. A. Knapp, J. T. Maxwell, W. P. Tyminski, and P. T. Soulé (2011), Ocean–atmosphere influences on low-frequency warm-season drought variability in the Gulf Coast and Southeastern United States, *Journal of Applied Meteorology and Climatology*, 50(6), 1177-1186, doi: 10.1175/2010jamc2566.1.
- Özger, M., A. K. Mishra, and V. P. Singh (2012), Long lead time drought forecasting using a wavelet and fuzzy logic combination model: A case study in Texas, *Journal of Hydrometeorology*, 13(1), 284-297.

- Palmer, W. C. (1965), Meteorological drought, US Department of Commerce, Weather Bureau Washington, DC. 56 pp.
- Patricola, C. M., P. Chang, and R. Saravanan (2013), Impact of Atlantic sst and high frequency atmospheric variability on the 1993 and 2008 Midwest floods: Regional climate model simulations of extreme climate events, *Climatic Change*, 129(3-4), 397-411, doi: 10.1007/s10584-013-0886-1.
- Penman, H. L. (1948), Natural evaporation from open water, bare soil and grass, paper presented at Proceedings of the Royal Society of London A: Mathematical, Physical and Engineering Sciences, The Royal Society, 120-145.
- Percival, D. B., and A. T. Walden. (1993), Spectral analysis for physical applications, Cambridge University Press. 583 pp.
- Schaake, J., T. Hamill, R. Buizza, and M. Clark (2007), Hepex: The hydrological ensemble prediction experiment, *Bulletin of the American Meteorological Society*, 88(10), 1541.
- Schlesinger, M. E., and N. Ramankutty (1994), An oscillation in the global climate system of period 65-70 years, *Nature*, 367(6465), 723-726.
- Silverman, D., and J. A. Dracup (2000), Artificial neural networks and long-range precipitation prediction in California, *Journal of Applied Meteorology*, 39(1), 57-66.
- Smith, C. A., and P. D. Sardeshmukh (2000), The effect of ENSO on the intraseasonal variance of surface temperatures in winter, *International Journal of Climatology*, 20(13), 1543-1557, doi: 10.1002/1097-0088(20001115)20:13<1543::AID-JOC579>3.0.CO;2-A.
- Stahle, D., and M. Cleaveland (1998), Texas drought history reconstructed and analyzed from 1698 to 1980, *Journal of Climate*, 1, 59-74.
- Sunghee, K., D.-J. Seo, H. Sadeghi, A. Philpott, F. Bell, J. Brown, A. Winguth, N. Fang, L. Baylock, G. Clingenpeel, and T. Fincannon (2016), Climate forecast-aided drought decision support

- for North Central Texas, poster presented at 96th American Meteorological Society Annual Meeting, 10-14 January.
- Torres, A. F., W. R. Walker, and M. McKee (2011), Forecasting daily potential evapotranspiration using machine learning and limited climatic data, *Agricultural Water Management*, 98(4), 553-562.
- Trajkovic, S., B. Todorovic, and M. Stankovic (2003), Forecasting of reference evapotranspiration by artificial neural networks, *Journal of Irrigation and Drainage Engineering*, 129(6), 454-457.
- van Loon, H., and J. C. Rogers (1978), The seesaw in winter temperatures between Greenland and Northern Europe. Part i: General description, *Monthly Weather Review*, 106(3), 296-310, doi: 10.1175/1520-0493(1978)106<0296:TSIWTB>2.0.CO;2.
- Vaughan, E. (2012), *Water for Texas, Rep.*, TEXAS WATER DEVELOPMENT BOARD, Texas, pp. 1- 314.
- Venegas, S. A., and L. A. Mysak (2000), Is there a dominant timescale of natural climate variability in the Arctic?, *Journal of Climate*, 13(19), 3412-3434, doi: 10.1175/1520-0442(2000)013<3412:ITADTO>2.0.CO;2.
- Vicente-Serrano, S. M., S. Beguería, and J. I. López-Moreno (2010), A multiscalar drought index sensitive to global warming: The standardized precipitation evapotranspiration index, *Journal of Climate*, 23(7), 1696-1718.
- Vicente-Serrano, S. M., S. Beguería, J. I. López-Moreno, M. Angulo, and A. E. Kenawy (2010), A new global 0.5° gridded dataset (1901–2006) of a multiscalar drought index: Comparison with current drought index datasets based on the palmer drought severity index, *Journal of Hydrometeorology*, 11(4), 1033-1043, doi: 10.1175/2010jhm1224.1.

- Wallace, J. M., and D. S. Gutzler (1981), Teleconnections in the geopotential height field during the Northern Hemisphere winter, *Monthly Weather Review*, 109(4), 784-812, doi: 10.1175/1520-0493(1981)109<0784:TITGHF>2.0.CO;2.
- Winguth, A., J. H. Lee, and Y. Ko (2015), Climate change/extreme weather vulnerability and risk assessment for transportation infrastructure in Dallas and Tarrant counties, *Rep.*, North Central Texas Council of Governments, pp. 1-53.
- Wolf, J. W. (2012), Evaluation of drought metrics in tracking streamflow in Idaho, M.S thesis, 38 pp. University of Idaho, Moscow, July.
- Wu, Z., Y. Mao, X. Li, G. Lu, Q. Lin, and H. Xu (2016), Exploring spatiotemporal relationships among meteorological, agricultural, and hydrological droughts in Southwest China, *Stochastic Environmental Research and Risk Assessment*, 30(3), 1033-1044, doi: 10.1007/s00477-015-1080-y.
- Wyatt, M. G., S. Kravtsov, and A. A. Tsonis (2011), Atlantic Multidecadal Oscillation and Northern Hemisphere's climate variability, *Climate Dynamics*, 38(5-6), 929-949, doi: 10.1007/s00382-011-1071-8.
- Yamamoto, A., and J. B. Palter (2016), The absence of an Atlantic imprint on the Multidecadal variability of wintertime European temperature, *Nature Communication*, 7, doi: 10.1038/ncomms10930.
- Zhang, Y., J. M. Wallace, and D. S. Battisti (1997), ENSO-like interdecadal variability: 1900–93, *Journal of Climate*, 10(5), 1004-1020, doi: 10.1175/1520-0442(1997)010<1004:ELIV>2.0.CO;2.
- Zwiers, F. W., and H. v. Storch (1999), *Statistical analysis in climate research*, Cambridge University Press, 496 pp.

Biographical Information

Tyler Fincannon graduated from The University of Texas at Dallas with a Bachelor's of Science in Geology after completing a major in Geophysics. After obtaining his B.S. he pursued and completed his Masters of Science in Geology at the University of Texas Arlington. He joined the Climate Research Group in the Department of Earth and Environmental Sciences in pursuit of his interest in the mitigation of future climate events, due to changing climate conditions from anthropogenic activity. While working towards his masters, he functioned as a graduate teaching and research student for Dr. Arne Winguth, Associate Professor, in the field of regional hydrology; working to improve regional predictions of meteorological drought conditions under a grant funded by NOAA, and set up several high-performance DELL computer servers for the entire research group. His research was accepted for oral presentation at the 2017 annual meeting of the American Meteorological Society. He is a student member of multiple professional organizations such as the American Meteorological Society, the Geological Society of America, and the Association of Environmental/Engineering Geologists. After completion of his master's degree in May of 2017, Tyler Fincannon plans to enter the federal or private sector and continue his efforts in assisting communities in the adaptation to impacts from climate variations and change.